


**Universality of modular symmetries in two-dimensional magnetotransport**

K. S. Olsen, H. S. Limseth, and C. A. Lütken

*Department of Physics, University of Oslo, NO-0316 Oslo, Norway* (Received 11 August 2017; revised manuscript received 27 November 2017; published 10 January 2018)

We analyze experimental quantum Hall data from a wide range of different materials, including semiconducting heterojunctions, thin films, surface layers, graphene, mercury telluride, bismuth antimonide, and black phosphorus. The fact that these materials have little in common, except that charge transport is effectively two-dimensional, shows how robust and universal the quantum Hall phenomenon is. The scaling and fixed point data we analyzed appear to show that magnetotransport in two dimensions is governed by a small number of universality classes that are classified by *modular* symmetries, which are infinite discrete symmetries not previously seen in nature. The Hall plateaux are (infrared) stable fixed points of the scaling-flow, and quantum critical points (where the wave function is delocalized) are unstable fixed points of scaling. Modular symmetries are so rigid that they in some cases fix the global geometry of the scaling flow, and therefore predict the exact location of quantum critical points, as well as the shape of flow lines anywhere in the phase diagram. We show that most available experimental quantum Hall scaling data are in good agreement with these predictions.

DOI: [10.1103/PhysRevB.97.045113](https://doi.org/10.1103/PhysRevB.97.045113)**I. INTRODUCTION AND SUMMARY**

The continuous and discrete symmetries observed in nature may be exact or approximate. The continuous case includes exact symmetries like Lorentz and gauge invariance, which severely constrains possible dynamical models, while discrete symmetries usually are finite and approximate. We shall here investigate a class of experimental data that appear to respect a new type of symmetry that is called *modular*. Although these are finitely generated approximate (emergent) discrete symmetries, because they are non-Abelian and infinite, they provide unusually strong constraints on low-energy model building.

Infinite discrete groups, including modular symmetries, play an important role in modern mathematics, but because they are extremely rigid, it is not clear if they can exist in the real physical world. Indeed, it is only in bespoke physical systems (“designer universes”), engineered to be effectively (for all practical purposes) two-dimensional, that modular symmetries have been found [1–26].

The quantum Hall effect (QHE) appears in materials where charge carriers are forced to move in a single atomic plane, for example, on the surface of a crystal or in a sheet of graphene. Experiments measuring the electromagnetic properties (magnetotransport) of Hall systems produce what at first sight appears to be an impenetrable morass of data. However, first appearances can be misleading, and if the quantum Hall data are viewed from a particularly advantageous vantage point, a hidden pattern of great beauty and utility is revealed [1,2]. This rigid emergent order is encoded in a fractal phase diagram tightly harnessed by a modular symmetry that allows it to teeter on the brink of chaos, without actually taking the leap.

Our purpose here is to explore the robustness and universality of these new symmetries, by comparing and contrasting data from the most disparate materials available. We do this in the simplest possible way, by superimposing scaling data directly onto mathematical diagrams with modular symmetry. This “phenomenological” approach is unbiased, since no the-

oretical assumptions are invoked, and we are free to represent (plot) the data in any way we want. We will not here discuss theoretical ideas that are needed in order to connect the well-known microphysics (“electrons in a dirty lattice”) to the emergent macrophysics observed in transport experiments.

Since modular mathematics is unfamiliar to most physicists, a brief introduction to modular symmetry in physics is provided in the next section. In order to motivate this, we start by summarizing the main conclusion: *the scaling properties of a quantum Hall system appears to have a remarkable simplicity and universality encoded in a modular symmetry.*

More precisely, the Hall and magnetoconductivities  $\sigma_H$  and  $\sigma_D$  show a strong dependence on the dominant scale parameter  $t$  (usually temperature), and the *scaling functions*  $\beta_H = d\sigma_H/dt$  and  $\beta_D = d\sigma_D/dt$  appear to be harnessed by a modular symmetry. Provided that these functions have certain analyticity properties, the modular symmetry is so rigid that they only barely survive; (i) if the symmetry observed in an experiment is one of the maximal subgroups of the modular group, then *the physical  $\beta$  function is unique*, up to an overall normalization (cf. Fig. 2), and (ii) if the symmetry observed in an experiment is the largest subgroup shared by the maximal subgroups, then *there is a unique family of  $\beta$  functions parametrized by a single real number*, up to an overall normalization (cf. Fig. 4). These all but unique  $\beta$  functions generate equally unique flow diagrams, which we compare with scaling data. They almost always agree, within the experimental error (cf. Figs. 6–17).

This transmutation of modular mathematics into quantum Hall physics follows from a fundamental property of scaling functions: *they must respect any geometric structure with which the parameter space is endowed.* In the QHE, this is the space of transport coefficients (conductivities or resistivities), which appears to be equipped with both a *complex structure* and an *emergent modular symmetry*. These circumstances conspire to give a very strong constraint on low-energy physics,

and any model of this physics, as we now explain in the context of the QHE.

It is convenient to combine the real conductivities  $\sigma_H$  and  $\sigma_D$  into a complex quantity  $\sigma = \sigma_H + i\sigma_D$  that takes values in the upper half of the complex plane:  $\sigma \in \mathbb{C}^+$  ( $\Im\sigma = \sigma_D > 0$ ). This is useful because it reduces (transport) matrix operations to ordinary (complex) algebra, but an examination of the geometric properties of the scaling flow reveals a more profound reason to use complex coordinates: they are inescapable if the scaling flow is irrotational and incompressible. Why this should be the case may be motivated by some empirical observations that constrain the complexified scaling function  $\beta = d\sigma/dt = \beta_H + i\beta_D = (\beta_H, \beta_D)$ , which is a tangent vector field on the parameter space.

The first condition is that  $\beta$  should be curl free, which means that it is a gradient flow derived from a scalar potential. This eliminates limit cycles, which are never seen, presumably because they would render the conventional physical interpretation of the potential as counting (effectively massless) degrees of freedom meaningless. In other words, this condition is consistent with experimental reality, and it is needed for the scaling flow to adhere to conventional wisdom about renormalization.

The second condition is that  $\beta$  should be finite on  $\mathbb{C}^+$ , except for simple zeros at quantum critical points. This means that there are no sources or sinks (singularities) on  $\mathbb{C}^+$ , so the flow is incompressible and divergence free.

If this condition is not used, as has been tried in the past [27], much more complicated flows than those discussed here are possible. However, we are not aware of any evidence suggesting that there are sources or sinks for the scaling flow not on the boundary of parameter space. Furthermore, since it appears that our much more restrictive framework is sufficient to account for virtually all scaling data, we will not relax this condition.

Demanding that a vanishing point of  $\beta$  be simple means that it is a regular saddle point for the flow, as required for a normal critical point. Again this condition is needed for the scaling flow to adhere to conventional wisdom about renormalization.

Demanding that  $\beta$  be free of curl and divergence severely constrains the geometry of the flow because this is (in two dimensions) equivalent to the Cauchy-Riemann equations. It follows that  $\beta$  is a holomorphic function of  $\bar{\sigma}$ , i.e., antiholomorphic in  $\sigma$  [28]. Such *Laplacian flows* are automatically gradient flows, i.e., completely determined by a scalar potential  $\varphi$ , which in this context is called the *renormalization group (RG) potential* or *C function* [cf. Eq. (2)].

These constraints are arguably physically sensible and/or well founded in empirical data, but they are far from obvious. It would be prudent at this stage to treat them as (reasonable) assumptions whose veracity may or may not be confirmed by confronting their consequences with experimental data. In other words, this is an ansatz that will be validated *a posteriori*. At the very least, it provides motivation and a conceptual framework for pondering the origin of these unusual symmetries and their “unreasonable effectiveness” in organizing quantum Hall data.

Formulating the next condition requires a new vocabulary that is used in the theory of infinite groups. In order not to interrupt this summary, we postpone many definitions until the

next (more formal) section, after which the reader may wish to revisit this narrative. The third condition is that  $\beta$  should have some type of *modular symmetry*. This is at present a purely empirical observation, with little or no theoretical foundation. Combined with complex analyticity (the Cauchy-Riemann equations), we may conclude that  $\beta$  is a *modular form of weight two*.

It is the paucity of weight two forms on large modular groups that gives modular symmetry extremely sharp teeth. The first useful result is that *no* such forms exist if  $\Gamma$  is the full modular group  $\Gamma(1)_0 = \text{SL}(2, \mathbb{Z})$ , and there are therefore no candidate  $\beta$  functions with this symmetry. This provides a theoretical reason, independent of the experimental observation that this symmetry is too large, for considering smaller groups. So we turn our attention to subgroups of  $\Gamma(1)_0$ , where further surprises await us [29], including (i) and (ii).

We shall see that this provides a host of rigid predictions that are easy to falsify. The most surprising consequence of a modular symmetry is perhaps that the plateaux *must* be rational. This follows from the fact that in order for a modular symmetry to act “properly” on the real line (in a strict mathematical sense) [30], the upper half plane  $\mathbb{C}^+$  is compactified to the *extended upper half-plane*  $\bar{\mathbb{C}}^+$  by adding *only* rational numbers, and the point at infinity:  $\bar{\mathbb{C}}^+ = \mathbb{C}^+ \cup \mathbb{Q} \cup \{i\infty\}$ . It is also appealing that the integer (IQHE) and fractional (FQHE) quantum Hall effects are automatically unified by a modular symmetry.

The crux of the mathematical primer in Sec. II is Fig. 2, which shows all viable phase diagrams that are consistent with maximal modular symmetry, and Fig. 4, which shows how these fit snugly into a one-parameter family of quantum Hall phase diagrams with the slightly smaller symmetry  $\Gamma(2)$ . It should be possible to skip most of the mathematics, retaining only this atlas of modular maps, in order to follow the phenomenological analysis of experimental data in the bulk of this work.

This section is followed by some introductory remarks about the novel materials that have yielded most of the new data discussed in the following sections. They give a fairly comprehensive overview of the current experimental status of the modular hypothesis, including all scaling experiments we have found to be of sufficient quality to enable us to extract a partial flow diagram. Sections IV–VII provide what is essentially a catalog of fixed point data and scaling diagrams, organized by the modular symmetry they exhibit. Within each of these universality classes, the data are grouped according to the type of material used in the experiment. Section VIII summarizes previous work and some of the successes of the modular paradigm so far, as well as some of the outstanding problems and challenges to be addressed in future work.

## II. MODULAR SYMMETRY

The idea to be investigated here is that a two-parameter scaling theory suffices to describe the QHE at low energy where transport experiments are performed. These parameters are the scale dependent conductivities, and since  $\sigma_D \geq 0$  they take values in  $\mathbb{C}^+(\sigma = \sigma_H + i\sigma_D)$ . As long as the inelastic scattering length is smaller than the size of the Hall bar, the dominant scale parameter is the temperature  $T$ . The phase and flow diagrams on display in this article are obtained by

studying families  $\sigma(T; B, \dots)$  of quantum Hall data, where  $B$  is the magnetic field strength and the ellipsis represents other nonuniversal quantities that depend on the type of material used. Before doing so, we give a brief glossary of the vernacular used in the theory of scaling and renormalization, and throughout this paper (*italics* signals that the term is defined by the sentence in which it appears). Most of it is borrowed from hydrodynamics.

A *flow line* tracks how the effective (renormalized) values of the transport coefficients change when the scale parameter (temperature) is changed. We are free to dial any starting point for a flowline by changing nonscale parameters, like the magnetic field  $B$ , which must subsequently remain fixed while only the scale parameter is changed.

A *flow diagram* is a collection of such flow lines, which if possible are chosen so that they “spread out” and probe as much of parameter space as possible (in practice experimental limitations severely constrains access to initial values). Since flow lines cannot cross phase boundaries they chart the phase diagram. The geometry of any flow diagram is controlled by *fixed points* of the flow, i.e., points in parameter space where the flow (scaling) stops, so they are by definition scale invariant.

Sinks for the flow are called *attractive infrared (IR) fixed points*, which we represent by the icon  $\oplus$ . In the QHE, these are the plateaux, where  $\sigma_H$  is a rational number ( $\in \mathbb{Q}$ ) in units with  $e^2/h = 1$ , and  $\sigma_D$  vanishes. Rational points should therefore be included in the physical parameter space for the QHE. In mathematics, this is called a *compactification* of the open set  $\mathbb{C}^+$  to  $\overline{\mathbb{C}^+}$ . For topological reasons, only rational points may be added (including the “fraction”  $\infty = 1/0$ ), and they are called the *boundary* of  $\overline{\mathbb{C}^+}$ .

Sources for the flow are called *repulsive ultraviolet (UV) fixed points*, which we represent by the icon  $\ominus$ . Experiments reveal that these fixed points also lie on the boundary of parameter space.

Saddle points for the flow (one attractive and one repulsive direction) are called *semistable fixed points*, which we represent by the icon  $\otimes$ . In the QHE, these are the quantum critical points that control quantum phase transitions, sometimes called the localization-delocalization transition, between phases “attached” to different plateaux. Physical critical points are vanishing points (zeros) of the vector field  $\beta = (\beta_H, \beta_D)$  of scaling functions, which belong to the interior of parameter space.

This fixed point structure can be extracted directly from the geometry of the data without any theoretical bias. If they reveal a hidden order (symmetry), then they are the DNA of this symmetry from which all else will follow. Our main assertion is that quantum Hall data does reveal such an order, encoded in the nested hierarchical structure of phase portraits (cf. Figs. 6–17). This is the signature of an approximate global discrete symmetry, which, given some familiarity with infinite discrete groups, is surprisingly easy to identify by finding some of the fixed points. The symmetry in question is called *modular*.

A *modular transformation* is a special type of Möbius transformation, familiar from complex analysis, which is a fractional linear map  $z \rightarrow (az + b)/(cz + d)$  of the complex plane  $\mathbb{C}(z)$  onto itself. Recall that such maps preserve angles but not lengths. If  $a, b, c, d$  are integers, and  $ad - bc = 1$ , then

this transformation preserves the upper half  $\mathbb{C}^+$  of the complex plane. The set of all transformations restricted in this way (there are infinitely many) form a group, called *the modular group*  $\Gamma(1) = \text{SL}(2, \mathbb{Z})$ . It is generated by a (horizontal) *translation*  $T(z) = z + 1$ , and a *duality transformation*, which in this case is the inversion (“reflection”)  $S(z) = -1/z$  in the unit circle. Since the *generators*  $T$  and  $S$  do not commute, e.g.,  $TS(z) = (z - 1)/z \neq -1/(z + 1) = ST(z)$ , this is an infinite, discrete, non-Abelian group that we sometimes write as  $\langle T, S \rangle$ .

Subgroups are easily obtained by restricting the coefficients  $a, b, c$ , and  $d$  further. For example, if  $a$  and  $d$  are required to be odd and  $b$  and  $c$  are even (the matrix  $(a, b; c, d) = \mathbf{1} \pmod{2}$ ), this gives the important *principal congruence subgroup at level two*, usually called  $\Gamma(2)$ , which will play an important role in the following.

There are larger subgroups of  $\Gamma(1)$  that contain  $\Gamma(2)$ , three of which we will call the *maximal subgroups*  $\Gamma_R$ ,  $\Gamma_S$ , and  $\Gamma_T$ . They are uniquely defined by how they are generated, as shown below in Eq. (1), or, equivalently, by how they group together rational numbers into equivalence classes (closed sets) under the transformations in the group. The latter is particularly useful, since it is the plateaux spectrum (a set of rational numbers) that is the most obvious property of a universality class.

For example, if  $T : z \rightarrow z + 1$  belongs to the symmetry group, then since  $\dots \xrightarrow{T} -2 \xrightarrow{T} -1 \xrightarrow{T} 0 \xrightarrow{T} 1 \xrightarrow{T} 2 \xrightarrow{T} \dots$ , all integers are equivalent under the symmetry, and consequently all integer plateaux must appear on an equal footing in the phase diagram. This transformation preserves the parity of the denominator (integers  $n = n/1$  all have odd denominator, and in general  $p/q \xrightarrow{T} p/q + 1 = (p + q)/q$  preserves the denominator  $q$ ).

As far as the full modular group  $\Gamma(1)$  is concerned, all fractions (plateaux values) are equivalent, i.e., given any two rational numbers there is always some transformation in  $\Gamma(1)$  that takes one into the other. Consequently, if this were a physically viable symmetry for the QHE we should observe all possible fractional plateaux. However, we never observe the full set of fractions in any given quantum Hall experiment, but only plateaux (fractions) that satisfy certain constraints on the parities of the numerator, or denominator, or both.

These *parity rules*, which depend on the two-dimensional material under consideration, is the key to identifying any would-be modular symmetry. They link microphysics to macrophysics, because the observed spectrum of integer fixed points follows directly from the spectrum of charge carriers supported by the system in the noninteracting limit (“Landau level spectroscopy”).

The resistivity  $\rho = S(\sigma) = -1/\sigma$  is conveniently given by the modular duality transformation  $S$ , since this is equivalent to taking the matrix inverse of the conductivity tensor. Note that it is conventional to choose  $\sigma_H = \sigma_{12}$  and  $\rho_H = \rho_{21}$  in order to eliminate an annoying minus sign.

### A. Hierarchy of symmetries

So the full modular symmetry is too strong for the QHE, but the largest subgroups of  $\text{SL}(2, \mathbb{Z})$  are not. A map showing the tip of the modular iceberg, including all the groups we need, is presented in Fig. 1. Lines between groups indicate

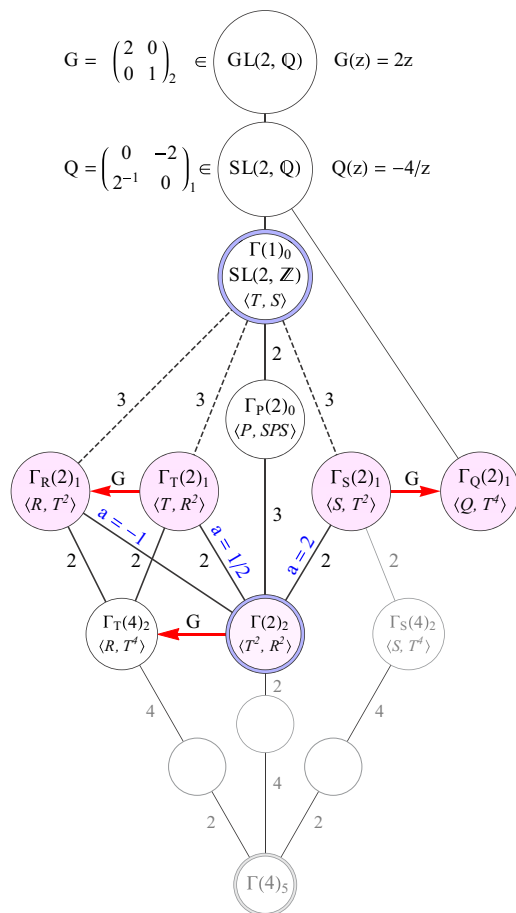


FIG. 1. Some of the groups between  $GL(2, \mathbb{Q})$  and  $\Gamma(4)$  that are relevant for the QHE. Lines connect a subgroup to its parent groups higher up in the hierarchy. (A thick solid line means that the subgroup is normal, and the index of the subgroup labels the line, but this will not be used here.) There are another twenty groups between  $\Gamma(1)_0 = SL(2, \mathbb{Z})$  and  $\Gamma(4)_5$  that are not shown here [31,32]. Both  $\Gamma(1)_0$  and  $\Gamma_p(2)_0$ , where  $P = ST$  ( $P^3 = 1$ ), are too large to support a physical  $\beta$  function. The pink groups are not too big, and it is their flow diagrams that we compare to experiments.

that the lower one is a subgroup of the upper one. One way to obtain a subgroup of the modular group is to relax the translation symmetry ( $T \rightarrow T^n$ , for  $n = 2, 3, \dots$ ), the duality symmetry [ $S \rightarrow R^n$ , where  $R(z) = TST(z) = z/(1+z)$ ], or both. Three of these so-called “congruence subgroups at level two” preserve parities, which means that each of them groups the fractions into two equivalence classes. Because  $p$  and  $q$  in  $\sigma_{\oplus} = p/q$  are relatively prime, there are only three types of fractions with well defined parities.

With “ $o$ ” representing odd integers and “ $e$ ” representing even integers, we have  $p/q \in o/o, o/e$  or  $e/o$ , and it is easy to verify that the equivalence classes are [33]

$$\begin{aligned} \Gamma_T &= \Gamma_T(2)_1 = \langle T, R^2 \rangle : \left\{ \frac{e}{o}, \frac{o}{o} \right\}_{\oplus} \cup \left\{ \frac{o}{e} \right\}_{\ominus}, \\ \Gamma_R &= \Gamma_R(2)_1 = \langle R, T^2 \rangle : \left\{ \frac{e}{o} \right\}_{\oplus} \cup \left\{ \frac{o}{o}, \frac{o}{e} \right\}_{\ominus}, \\ \Gamma_S &= \Gamma_S(2)_1 = \langle S, T^2 \rangle : \left\{ \frac{o}{o} \right\}_{\oplus} \cup \left\{ \frac{o}{e}, \frac{e}{o} \right\}_{\ominus}. \end{aligned} \quad (1)$$

A class is indexed by  $\oplus$  if the fractions are attractive fixed points of scaling in the  $\sigma$  plane, and by  $\ominus$  if they are repulsive fixed points. This assignment follows from the requirement that the direction of the flow is downward at the top of the conductivity plane, which is a result that can be obtained in a perturbative analysis of localisation in the weak coupling limit  $\sigma \rightarrow i\infty$ . The fixed point at vanishing coupling must therefore be repulsive,  $i\infty = \ominus$ . Since  $\infty = 1/0 \in o/e$ , and all fixed points in a given class are mapped into each other by the symmetry, all fractions in the class containing  $o/e$  must be repulsive. Notice that the denominators of attractors always are odd.

Figure 1 shows some of the groups between  $GL(2, \mathbb{Q})$  and  $\Gamma(4)_5$ . The subscript is the number of linearly independent  $\beta$  functions that the symmetry allows [34]. We know the dimension of this vector space because  $\beta$  must transform as a vector, also under modular transformations. In mathematics this is called a modular form of weight 2, and the number of such functions has been tabulated for the most common groups [32].

The red arrow is a *modular correspondence* obtained by conjugating with  $G \in GL(2, \mathbb{Q})$ , where  $G(z) = 2z$ . The relation  $\Gamma_T(4)_2 = G \Gamma(2)_2 G^{-1}$  is important in the theory of theta-functions (modular forms of weight  $w = 1/2$ ) [35]. Conjugating  $\Gamma_T(2)_1$  gives the familiar group  $\Gamma_R(2)_1 = G \Gamma_T(2)_1 G^{-1}$ , but  $\Gamma_Q(2)_1 = G \Gamma_S(2)_1 G^{-1}$  is new. The  $G$  conjugate  $Q = GS^{-1}(z) = -4/z$  of the duality generator  $S$  is a (non-normalized) *Fricke involution*.  $G$  changes or *transmutes* a modular symmetry into an equivalent group, rather than *breaking* it to a smaller subgroup. This corresponds to moving horizontally and vertically in Fig. 1.

The symmetries that have been found to be relevant for the QHE are colored pink. When  $a = -1, 1/2$ , and  $2$ , the symmetry of the  $\Gamma(2)_2$ -invariant RG potential  $\varphi_a$  discussed below (cf. Sec. IIC and Fig. 4) is enhanced to one of the maximal subgroups of  $\Gamma(1)_0$ , as indicated on the diagram.  $\Gamma_X(2)_1$  ( $X = Q, R, T$ ) are the symmetries most often observed in experiments. Since only level two appears to be physically relevant (so far), we often simplify notation by dropping the level [ $\Gamma_X = \Gamma_X(2)_1$ ].

## B. Modular phase diagrams

So far, we have only discussed how the symmetries act on the plateaux. We now extend this into the interior of parameter space, i.e., we review how modular symmetries partitions all of  $\overline{\mathbb{C}}^+$ , not just the points on the boundary.

Because the duality transformation  $S$  swaps  $e/o$  and  $o/e$ , leaving  $o/o$  unchanged, the direction of the flow in the  $\rho = S(\sigma)$  plane is reversed if the symmetry acting on  $\sigma$  is  $\Gamma_T$  or  $\Gamma_R$ , but not if the symmetry is  $\Gamma_S$  or  $\Gamma_Q$ . This dichotomy is a persistent theme.

The fixed point at the origin of the  $\sigma$  plane (at  $i\infty$  in the  $\rho$  plane) has a special significance. If it is attractive this means that the system has an insulating phase, which we call the quantum Hall insulator (QHI) and assign the special symbol  $\otimes$ . Since  $0 = 0/1 \in e/o$ , we conclude that a model with  $\Gamma_T$  or  $\Gamma_R$  symmetry in the  $\sigma$  plane does have this insulator phase, but that  $\Gamma_S$ - and  $\Gamma_Q$ -symmetric models do not (cf. Eq. (1) and Fig. 2).

Notice that all plateaux in the Hall conductivity are accompanied by vanishing magnetoconductivity ( $\sigma_D = 0 \Rightarrow \sigma_H \in \mathbb{Q}$ ), also for the insulator phase, as expected from naive

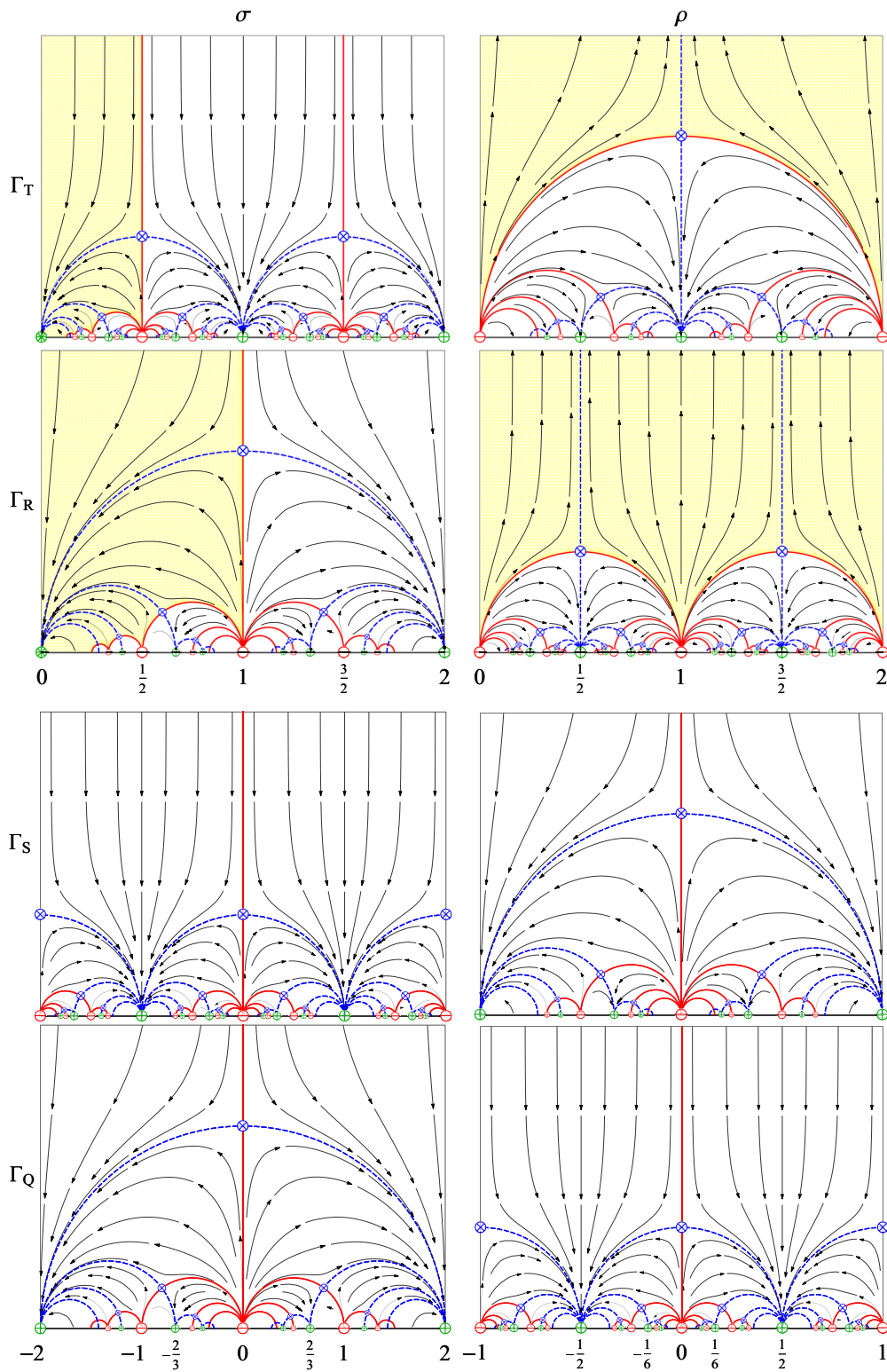


FIG. 2. Conductivity ( $\sigma$ ) and resistivity ( $\rho = -1/\sigma$ ) phase diagrams with symmetry  $\Gamma_X$  ( $X = Q, R, S, T$ ). Only  $\Gamma_T(\sigma)$  and  $\Gamma_S(\sigma)$  are truly different since  $\Gamma_R(\sigma)$  is simply a doubling of  $\Gamma_T(\sigma)$ , and likewise for  $\Gamma_Q(\sigma)$  and  $\Gamma_S(\sigma)$ . The main physical distinction is that  $\Gamma_T$  (and  $\Gamma_R$ ) has an insulator phase (yellow;  $\sigma_{\otimes} = 0, \rho_{\otimes} = i\infty$ ), while  $\Gamma_S$  (and  $\Gamma_Q$ ) does not.

localization theory (cf. Fig. 2). The same is true for the resistivities, except for the peculiar insulator phase ( $\rho_D = 0 \Rightarrow \rho_H \in \mathbb{Q} \neq 0$ ). In this case, the “plateau”  $\otimes = i\infty$  is associated

with a diverging magnetoresistivity, while the Hall resistivity is not quantized ( $\rho_D \rightarrow \infty \Rightarrow \rho_H \in \mathbb{R}$ ), because there is only one point at infinity in  $\overline{\mathbb{C}}^+$ .

TABLE I. (Left) Integer plateau values  $\oplus$  of the Hall conductivity  $\sigma_H$  constrained by a symmetry  $\Gamma(2) \subset \Gamma_X \subset \text{SL}(2, \mathbb{Q})$ , with  $X = Q, R, S$  or  $T$ , together with the location of semistable fixed points for transitions between these plateaux, i.e., the position of “integer” quantum critical points  $\otimes$  in the complexified conductivity plane. (Right) Corresponding values of the resistivity (see Sec. II for details).

IQHE	$\sigma = \sigma_H + i\sigma_D \in \overline{\mathbb{C}}^+(\sigma)$			$\rho = \rho_H + i\rho_D \in \overline{\mathbb{C}}^+(\rho)$		
$\Gamma_X$	$\oplus$	$\leftarrow \otimes \rightarrow$	$\oplus'$	$\oplus$	$\leftarrow \otimes \rightarrow$	$\oplus'$
$\Gamma_T$	$n$	$\frac{2n+1+i}{2}$	$n+1$	$\frac{1}{n+1}$	$\frac{2n+1+i}{2n^2+2n+1}$	$\frac{1}{n}$
$\Gamma_R$	$2n$	$2n+1+i$	$2n+2$	$\frac{1}{2n+2}$	$\frac{2n+1+i}{4n^2+4n+2}$	$\frac{1}{2n}$
$\Gamma_S$	$2n-1$	$2n+i$	$2n+1$	$\frac{1}{2n+1}$	$\frac{2n+i}{4n^2+1}$	$\frac{1}{2n-1}$
$\Gamma_Q$	$4n-2$	$4n+2i$	$4n+2$	$\frac{1}{4n+2}$	$\frac{2n+i}{8n^2+2}$	$\frac{1}{4n-2}$

The experimental signature of this phase is a plateau in the Hall conductivity with  $\sigma_H = 0$ , accompanied by a large *peak* in the magnetoresistivity,  $\rho_D \gg 1 [h/e^2]$ . This is, for example, what is observed experimentally when graphene is placed in a very strong magnetic field [36,37], signaling that the modular symmetry is changing from  $\Gamma_Q$  to  $\Gamma_T$ , as discussed in Sec. VII.

Observe also that  $\Gamma_R$  and  $\Gamma_T$  are conjugate inside the parent group  $\text{GL}(2, \mathbb{Q})$  under the rescaling  $G(z) = 2z$  by a factor of two (cf. Fig. 1). This means that flow diagrams with these two symmetries are identical, up to a doubling of all coordinates. A similar rescaling of  $\Gamma_S$  gives a conjugate group  $\Gamma_Q$  that is not strictly speaking modular (cf. Fig. 1), but its flow diagram is just a doubling of the  $\Gamma_S$ -symmetric flow.

In summary, since both  $\Gamma(1)_0$  and  $\Gamma_P(2)_0$  are too large, there are just two types of physically acceptable conductivity flow diagrams with maximal modular symmetry:  $\Gamma_T$  (and its  $G$ -conjugate  $\Gamma_R$ ), and  $\Gamma_S$  (and its  $G$  conjugate  $\Gamma_Q$ ). The former has an insulator phase, the latter does not.

For convenience, an “atlas” of  $Q$ -,  $R$ -,  $S$ -, and  $T$ -symmetric flows, in both  $\sigma$  and  $\rho$ , is provided in Fig. 2. In these cases, the shape of the flow lines (but not the flow rate) is completely fixed by the large symmetry. They are most easily derived as a gradient flow of RG potentials with the requisite symmetry [cf. Eq. (2)]. We defer details to the discussion below of symmetry transmutations.

For future reference we have also listed the integer fixed points for these cases in Table I. The complete spectrum of attractors (plateaux) for these symmetries may be found in Fig. 2.

$\Gamma_T$  and  $\Gamma_R$  are the relevant groups for respectively the ordinary spin-polarized and unpolarized QHE, where quasiparticles have the usual parabolic (“nonrelativistic”) dispersion, i.e., the QHE that appears in materials without Dirac modes. We will therefore call these the *nonrelativistic polarized and unpolarized groups*.

Graphene is different. Because of the peculiar topology of its Fermi surface, there is a doubling of degrees of freedom due to an additional “pseudospin” or “valley” degeneracy, and there are gapless (massless) excitations at half filling with linear dispersion, i.e., their energy is linear in momentum. These modes therefore behave like relativistic (Dirac) fermions, with the Fermi velocity replacing the speed of light. The linear

dispersion and unusual band structure leads to a different noninteracting spectrum, but that is all we need to identify the potential modular symmetry, and the phenomenological analysis of graphene is analogous to the parabolic case [12,13].

Note that a topological zero-mode eliminates the insulator phase, so the relevant groups in this “relativistic” case with Dirac modes are  $\Gamma_S$  and  $\Gamma_Q$ , for respectively the spin-polarized and unpolarized QHE. We will therefore call these the *relativistic polarized and unpolarized groups*.

A phase is by definition the set of all points in  $\overline{\mathbb{C}}^+$  that flow to a given plateau  $\oplus$  (IR fixed point), and it is uniquely labeled by this rational limit point on the real axis. A phase transition between two plateaux  $\oplus$  and  $\oplus'$  is permitted by the symmetry if it has a fixed point  $\otimes$  located on the semicircle in  $\overline{\mathbb{C}}^+$  connecting  $\oplus$  and  $\oplus'$ , which we write as  $\oplus \leftarrow \otimes \rightarrow \oplus'$  or  $\oplus \xleftrightarrow{\otimes} \oplus'$ . If one of the attractors is  $i\infty$  the semicircle has infinite radius, i.e., it is a vertical line. We also adopt the convention that  $\oplus \xleftrightarrow{\otimes} \oplus'$  refers to a transition in the conductivity plane, whence an integer plateau-value  $\oplus = \sigma_{\oplus} = \sigma_H = n[e^2/h] \in \mathbb{Z}$  refers to the IQHE, for which  $\rho_H = 1/n[h/e^2]$ .

### C. Transmutation of symmetries

Degeneracies in the spectrum of delocalized states may be broken either by external fields, or by internal many-body interactions between charge carriers within each band, or both. In the simplest materials, we only have spin-degeneracy to consider. A symmetry transmutation occurs when the spins are neither fully polarized, nor fully degenerate, in which case the modular symmetry is at least partially broken. The maximal groups are no longer relevant, but it is conceivable that some smaller symmetry survives. The simplest situation is if we have *minimal symmetry breaking*, which means that the largest common subgroup survives. From our map in Fig. 1, we see that this group is  $\Gamma(2)$ , and our task is to find a  $\Gamma(2)$ -symmetric family of physically sensible  $\beta$ -functions that interpolates between  $\Gamma_R$ ,  $\Gamma_T$  and  $\Gamma_S$ .  $\Gamma_Q$  is not in this family because it is not in the modular group  $\Gamma(1)$ .

$\Gamma(2)_2$  admits a two-dimensional vector space of weight two forms, which is spanned by two Jacobi theta functions, for example  $\theta_3^4$  and  $\theta_4^4$ . Since  $\theta_2^4$  is also a weight two form it must be somewhere in this space, and because  $\theta_2^4 = \theta_3^4 - \theta_4^4$  it is. Any  $\Gamma(2)$ -symmetric  $\beta$  function must be a linear combination of these [22]:

$$\begin{aligned} \beta_a &\propto (1-a)\theta_3^4 + a\theta_4^4 = \theta_3^4 - a\theta_2^4 \propto \partial\varphi_a, \\ \varphi_a &= \ln \lambda + (a-1)\ln(\lambda-1), \quad \lambda = \theta_2^4/\theta_3^4. \end{aligned} \quad (2)$$

This is, as expected, a gradient flow, derived from the  $\Gamma(2)$ -invariant RG potential  $\varphi_a$ . It interpolates between the maximally symmetric cases labeled R, S, and T, while retaining as much modular symmetry as possible [38]. The phenomenological parameter  $a$  has an unknown and presumably complicated dependence on nonuniversal microscopic details, like many-body interactions and Zeeman splitting. Provided we choose the normalization of  $\beta_a$  to be imaginary,  $a$  must be real for the flow to agree with perturbative localization theory at weak coupling ( $1/\sigma_D \rightarrow 0$ ).

The thousands of nonsemicircular flow lines, phase boundaries and separatrices shown in this article were all obtained directly from  $\varphi_a$  by numerical integration, for a handful of real values of  $a$ . This includes the 282 modular flow lines that are compared to 1 484 experimental data points in Figs. 6–17. In all but one case (cf. Fig. 17), the agreement is within the estimated experimental uncertainty, and the exception is probably not in the scaling domain. We find that 1 434 data points on 274 flow lines appear to be consistent with modular ( $\Gamma(2)$  or  $\Gamma_Q$ ) symmetry, for only a few (seven) real values of  $a$ , and most of these (1 295 data points on 243 flow lines) are consistent with one of the maximal symmetries  $\Gamma_X$  ( $X = Q, R, S, T$ ). It is this universality we wish to investigate here.

When  $a = 0, 1, \infty$ , the  $\beta$  function degenerates to one of the theta functions ( $\beta_0 \propto \theta_3^4$ ,  $\beta_1 \propto \theta_4^4$ , and  $\beta_\infty \propto \theta_2^4$ ), which are finite. So for these three exceptional values of  $a$  (and only these),  $\beta_a$  has no zeros, and the flow has no fixed points (critical points) in  $\mathbb{C}^+$ . This phenomenon is unavoidable, because the family has three subfamilies where the plateaux-structures are quite distinct. Consider, for example, the triplet of fixed points  $\sigma_* \in (0, 1, 2)$ . We have  $(0, 1, 2) = (\otimes, \ominus, \oplus)$  for  $a < 0$ ,  $(0, 1, 2) = (\otimes, \oplus, \oplus)$  for  $0 < a < 1$ , and  $(0, 1, 2) = (\ominus, \oplus, \ominus)$  for  $1 < a$  (cf. Fig. 3). At  $a = 0, 1$  the critical points disappear by merging with the fixed points  $\sigma_* \in (0, 1, 2)$ , allowing a phase to appear ( $\ominus \rightarrow \oplus$ ) or disappear ( $\oplus \rightarrow \ominus$ ), as shown schematically in Fig. 3.

Figure 4 shows the complete family of  $\Gamma(2)$ -symmetric flow diagrams for the range of most physical interest. Each subfamily has one member for which the symmetry is enhanced from  $\Gamma(2)$  to one of the maximal subgroups:  $\Gamma_R$  when  $a = -1$ ,  $\Gamma_T$  when  $a = 1/2$ , and  $\Gamma_S$  when  $a = 2$ . For example, a very strong magnetic field gives a large Zeeman splitting that leads to  $\Gamma_T$  symmetry in the nonrelativistic case. For weak fields, this symmetry is transmuted into an unpolarized spectrum,  $\Gamma_T \xrightarrow{G} \Gamma_R$ .

Each panel is labeled on the left by the symmetry of the flow, and on the right by a function proportional to the  $\beta$ -function that generates the flow. The yellow region is the insulator phase, which disappears when  $a > 1$ .

Only at the unphysical singular points  $a = 0, 1$  are there no quantum critical points. Slicing this “family plot” at any value of the symmetry-breaking parameter  $a \neq 0, 1$  gives a “warped” but physically sensible diagram, i.e. a scaling flow that is finite except for simple zeros (cf. Fig. 17). These are the *quantum critical points*, located at  $\sigma_\otimes = i K'(a^{-1})/K(a^{-1})$  and all its  $\Gamma(2)$  images, where  $K$  and  $K'$  are elliptic integrals of the first kind [22]. This family is sufficiently large to accommodate almost all quantum Hall data that we have examined so far (one possible exception is discussed in Sec. VII).

In some materials, the band structure is more subtle, with additional “competing” degeneracies, and the pattern of symmetry breaking may be more complicated. For example, the four-fold spin-pseudospin degeneracy in graphene giving rise to  $\Gamma_Q$  symmetry can be broken by internal many-body or external magnetic field interactions. Independently of the microscopic mechanism, Fig. 5 shows an idealized pattern of symmetry breaking that transmutes flow diagrams. In this scenario, bands split if degenerate spin or pseudospin states (or both) are resolved. When a band splits a new delocalized state

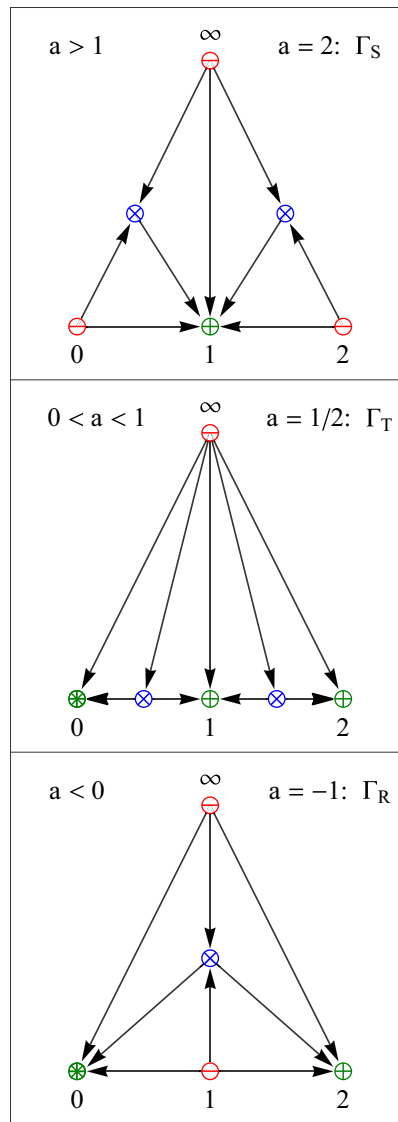


FIG. 3. Schematic of the three subfamilies of the  $\Gamma(2)_2$  family  $\varphi_a$ . Each of these has one (and only one) member with enhanced symmetry:  $\varphi_{-1}$  has  $\Gamma_R$  symmetry,  $\varphi_{1/2}$  has  $\Gamma_T$  symmetry, and  $\varphi_2$  has  $\Gamma_S$  symmetry (cf. Fig. 4). We call these subfamilies the R, T, and S families.

appears, giving rise to a new plateau in the Hall conductivity. Each symmetry (top row) has a unique spectrum of integer attractors (IQHE plateaux) (bottom row).

In real materials like graphene, many-body interactions, which presumably are responsible for pseudospin splitting, may obfuscate this simple picture. Since electron correlations appear to be strongest for the lowest Landau level, degeneracies may not be equally robust for all bands, leading to a hierarchy of plateaux spectra that only manifests a modular symmetry for limiting cases (strong and weak magnetic field, say). As in atomic physics, it may nevertheless be useful to retain the group theoretic labeling of states for intermediate cases where the symmetry is broken. Some graphene experiments exploring this question are discussed in the penultimate section.

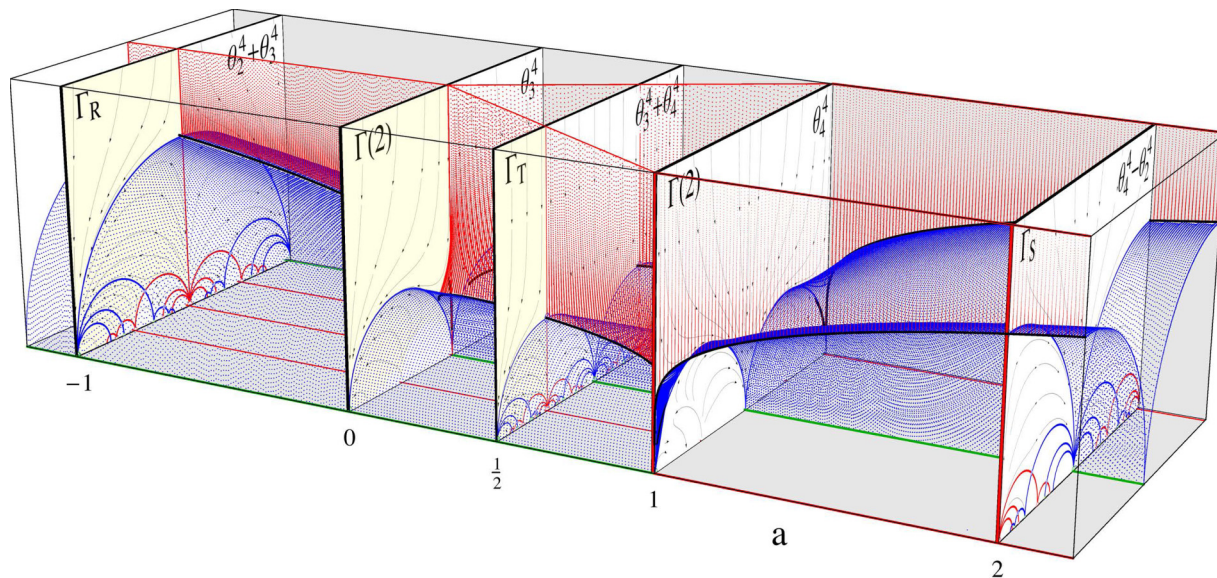


FIG. 4. The one-parameter family  $\beta_a$  of  $\Gamma(2)$ -symmetric RG flows, shown here for values of the symmetry-breaking parameter  $a$  in the range  $-1.2 < a < 2.2$ , is divided into three subfamilies by the “ramification points”  $a = 0, 1$ .

### III. NEW MATERIALS

We have argued that the convergence of modular mathematics and quantum Hall physics suggests that it would be unnatural to restrict attention to only one of the descendants of the modular group. We have also seen that there are very few viable candidates to choose from, and that most of these fit snugly into a simple and unique one-parameter family of  $\Gamma(2)_2$ -symmetric  $\beta$  functions (up to normalization). In other words, while these infinite non-Abelian symmetries are extremely constraining, they do leave enough flexibility that we can accommodate almost all experiments to date (but only barely so).

The discovery in recent years of new types of materials that support Dirac modes and “robust” topological edge states presents new opportunities for testing the modular paradigm sketched above. We will review a number of recent experiments that have explored large tracts of the modular landscape that were previously inaccessible.

These experiments have provided substantial evidence for those level two symmetries that until now have been beyond our reach. The data we have analyzed suggests that the full complement of level two symmetries may be present in nature. In preparation for that discussion, we give a brief summary of some of the most salient features of these materials.

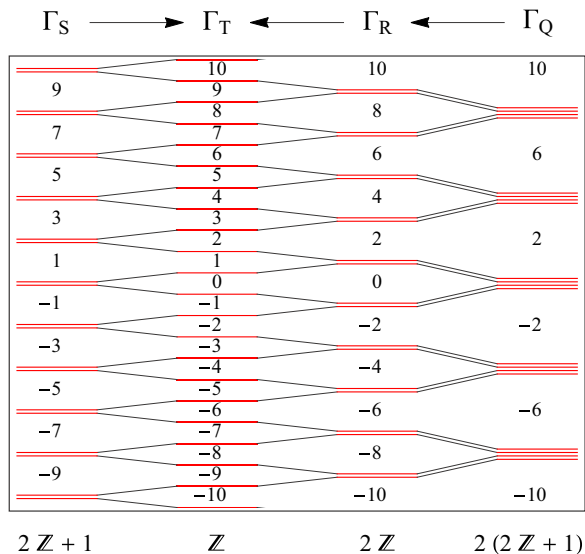


FIG. 5. Simplified pattern of symmetry transmutations from band splitting (lifting of spin and/or pseudospin degeneracies). Band gaps are labeled by the filling factor. Each symmetry  $\Gamma_X$  ( $X = Q, R, S, T$ ) leaves a unique fingerprint on the spectrum  $\oplus_X \in \mathbb{Q}$  of attractive fixed points, i.e., rational plateaux values of  $\sigma_H [e^2/h]$ .

#### A. Dirac matter

Dirac matter is a name used to describe materials in which the low-energy excitations are Dirac fermions. In Bloch theory, these states appear as a consequence of a finite number of crossing points in the Brillouin zone where the Hamiltonian becomes gapless. If the energy dispersion close to these points is linear, similar to the relativistic dispersion in particle physics, this is called a Dirac cone, and the effective low-energy Hamiltonian is Dirac-like, where the Fermi-velocity replaces the speed of light. When a Hall effect takes place in such materials, each zero mode contributes  $1/2$  to the Hall conductivity [39]. The Nielsen-Ninomiya theorem guarantees that Dirac cones come in pairs, ensuring an integral conductivity.

The most familiar material with linear (“relativistic”) dispersion is graphene, where two Dirac cones sit at corners of the Brillouin zone. In the presence of a magnetic field, each Dirac fermion contributes  $n + 1/2$  to the Hall conductivity. Taking into account both spin and valley (pseudospin) degeneracy the IQHE in graphene is  $\sigma_H = 4(n + 1/2) = 2 \pmod 4 \in \oplus_Q$  ( $n \in \mathbb{Z}$ ). The most unusual property of this plateaux spectrum is the absence of the attractor  $\oplus = 0$ , i.e., an insulator phase, which is a consequence of the zero modes shifting



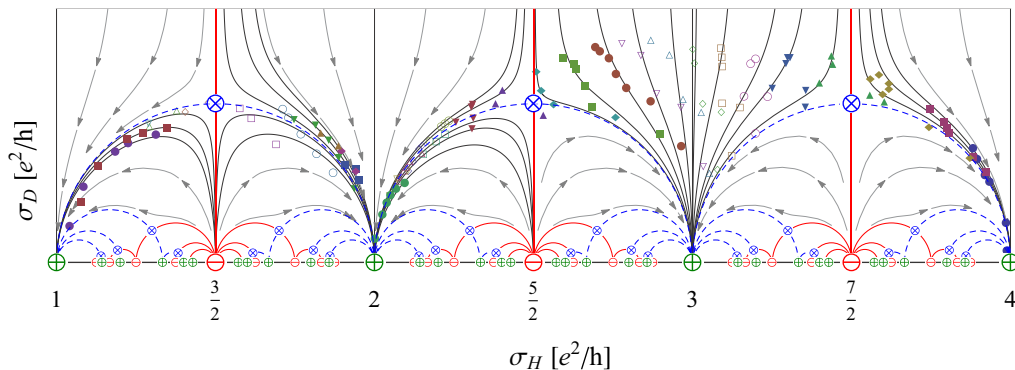


FIG. 6. Reconstruction of temperature-driven scaling data (discrete icons) exploring the plateau transitions  $1 = \oplus \leftrightarrow \otimes \oplus = 2 \leftrightarrow 3 = \oplus \leftrightarrow \otimes \oplus = 4$  in a semiconducting InGaAs/InP heterojunction [40].

the Hall spectrum. In the ordinary (un-)polarized IQHE, the plateau spectrum is  $\mathbb{Z}$  ( $2\mathbb{Z}$ ) =  $0 \pmod{1}$  ( $2$ ).

### B. Topological insulators

Topological insulators are special phases of matter characterized by a gapped bulk material with gapless edge or surface modes [41]. These gapless modes are topologically protected in the sense that they are robust to perturbations that preserve the symmetries of the system. The theory of topological insulators relies on Bloch theory as well as recent mathematical tools like Chern numbers and homotopy theory to characterize classes of Hamiltonians that preserve the bulk gap.

A normal insulator is said to be topologically trivial. The QED vacuum presents an insulator in this class. Here two bands are associated with electrons and positrons, while a large gap is associated with the pair production energy. The gapless surface modes of a topological insulator appear as a necessary consequence of a topologically nontrivial material ending on a trivial one (e.g., the vacuum). The only way a topological property can change across the interface is for the gap to close. This relation between bulk topology and edge modes are called the bulk-edge correspondence or duality.

The first topological insulator to be discovered was the IQHE itself. Here the Landau levels serve as energy bands, while a strong magnetic field induces a gap up to the first empty level. The bulk-boundary correspondence is in this case attributed to electrons skipping along the edges of the Hall sample due to the magnetic field. In this case, it is not the material that is considered a topological insulator but the IQHE as a whole.

Depending on the material in which the Hall effect takes place, different imprints are seen on the Hall conductivity. Graphene, for example, has a unique Hall spectrum  $\oplus_Q = 4n + 2$  due to its two Dirac cones.

Another example is provided by the surface of a three-dimensional topological insulator, which can serve as an effective two-dimensional arena for the QHE. The bulk-boundary correspondence tells us that this surface has massless excitations. Depending on the bulk topology the surface Brillouin zone has either an even or an odd number of Dirac cones [41], and the effective two-dimensional material can be seen as a Dirac material. In the case of an odd number of Dirac cones the Nielsen-Ninomiya theorem appears to be broken.

This is solved by the existence of partner Dirac fermions at the opposite surface of the three-dimensional topological insulator [41]. Under the assumption that the two sides are independent the Hall conductivity will be a sum of both contributions.

## IV. UNIVERSALITY CLASS $\Gamma_T$

### A. Plateaux transitions in InGaAs/InP

The result of the first scaling experiment in the context of the QHE, obtained in 1985 using a semiconducting heterojunction cooled below 4.2 K [40], is reconstructed in Fig. 6 from the published data. Clear indications of a modular symmetry are already evident in this diagram (cf. Fig. 2), even with the large uncertainty in the data.

Figure 6 shows our reconstruction of temperature-driven scaling data (discrete icons) exploring the plateau transitions  $1 = \oplus \leftrightarrow \otimes \oplus = 2 \leftrightarrow 3 = \oplus \leftrightarrow \otimes \oplus = 4$  in a semiconducting InGaAs/InP heterojunction with 2D electron density  $n = 3.4 \times 10^{11} / \text{cm}^2$ , mobility  $\mu = 35\,000 \text{ cm}^2/\text{Vs}$  and effective mass  $m^* = 0.047 m_e$  ( $m_e$  is the free electron mass), in the temperature range 4.2 K (top) to 0.5 K (bottom) [40]. Comparison with a modular scaling flow (solid lines) with quantum critical points at  $\otimes = 1/2, 3/2, \text{ and } 5/2$  reveals a  $\Gamma_T$  symmetry in the transport data (cf. Fig. 2).

In the three decades following this pioneering experiment, technology has improved and error bars have shrunk. In the following, we shall see that not only have experiments failed to contradict the symmetry, the agreement with the coldest experiments, where the symmetry is expected to be most accurate, is now in some cases at the per mille level.

### B. Plateaux transitions in GaAs/GaAlAs

Figures 7 and 8 provide further evidence for the existence of a universality class with  $\Gamma_T$  symmetry that unifies the IQHE (Fig. 8) with the FQHE (Fig. 7).

### C. Plateau-insulator transition in Cr(BiSb)Te

The QHE can take place on the top of three-dimensional topological insulators [44], like bismuth antimonide  $\text{Bi}_{1-x}\text{Sb}_x$  which was the first three-dimensional topological insulator to be discovered [45]. The effective edges of these

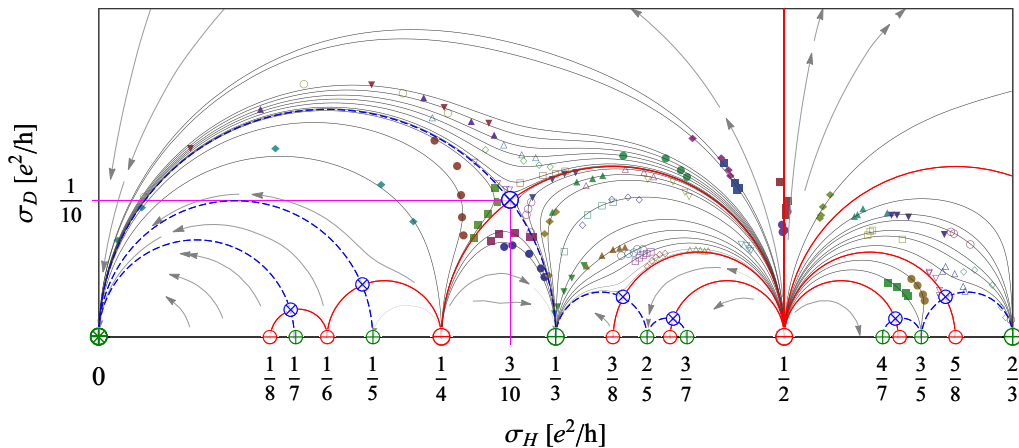


FIG. 7. Reconstruction of temperature-driven scaling data (discrete icons) exploring the fractional transitions  $0 = \oplus \leftrightarrow \ominus = 1/3 \xleftarrow{1/2} \ominus \rightarrow 3/5 = \oplus \leftrightarrow \oplus = 2/3$  in a GaAs/GaAlAs heterojunction [42].

two-dimensional surface systems are magnetic domain walls along which the charge carriers move.

Figures 9 and 10 show our reconstruction of temperature-driven scaling data (discrete icons) exploring the plateau-insulator transition  $0 = \oplus \leftrightarrow \oplus = 1$  in a 2D ferromagnetic topological insulator [thin film of  $\text{Cr}_x(\text{Bi}_{1-y}\text{Sb}_y)_{2-x}\text{Te}_3$  grown on a semi-insulating InP (111) substrate] [46]. After applying an external magnetic field  $B = 14$  T to saturate the magnetization, the magnetic field strength was set to zero and experiments were performed at different temperatures with tunable gate voltage. In order to compensate for what is presumably a systematic error of unknown origin, the data in Fig. 9 have been shifted slightly to the left so that the plateaux are integer-valued. In both cases, comparison with a modular scaling flow (solid lines) with a quantum critical point at  $\otimes = (1 + i)/2$  (cf. Table I and Fig. 2) reveals that these transport data are in excellent agreement with  $\Gamma_T$  symmetry.

#### D. Plateaux transitions in mercury telluride

Bulk mercury telluride is a semiconductor of the II-VI type [47], but when used to create a quantum well (HgCdTe/HgTe/HgCdTe) the electronic properties depend

crucially on the thickness  $d$  of the sample. This thickness introduces a parameter, which can be tuned to find quantum phase transitions. For thin wells with thickness below the critical thickness  $d_c \approx 6.3$  nm, the material has a normal band structure, whereas for wide wells ( $d > d_c$ ) the band structure is inverted [47,48].

In addition to having a highly specific energy spectrum with an inverted band structure, the 2DEG in a wide HgTe quantum well is characterized by a low effective mass,  $m^* = 0.02 m_e$  [49]. The low effective mass causes a large Landau level separation  $\Delta E = \hbar q B / m^* c$ , and the QHE survives to relatively high temperatures. In Refs. [50,51], a strong integer effect was observed up to  $T \sim 10\text{--}15$  K.

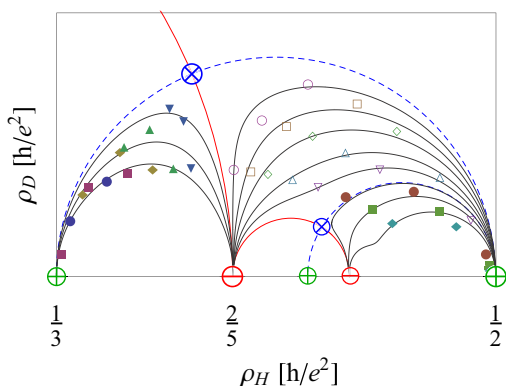


FIG. 8. Reconstruction of temperature-driven scaling data (discrete icons) exploring the plateaux transition  $2 = \oplus \leftrightarrow \oplus = 3$  in a GaAs/GaAlAs heterojunction [43].

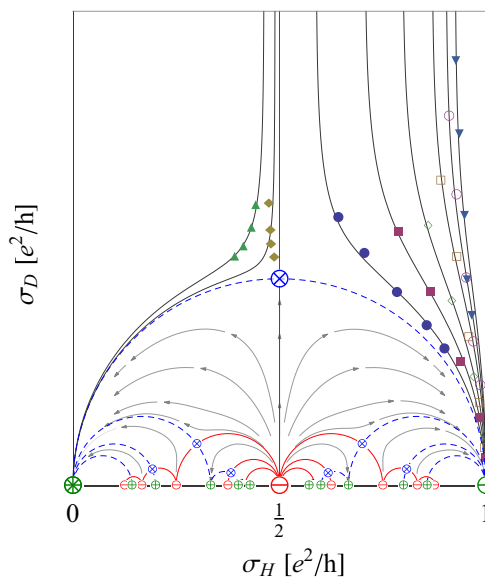


FIG. 9. Reconstruction of temperature-driven scaling data (discrete icons) exploring the plateau-insulator transition  $0 = \oplus \leftrightarrow \oplus = 1$  in a 2D ferromagnetic topological insulator (a thin film of  $\text{Cr}_x(\text{Bi}_{1-y}\text{Sb}_y)_{2-x}\text{Te}_3$  grown on a semi-insulating InP(111) substrate) [46].

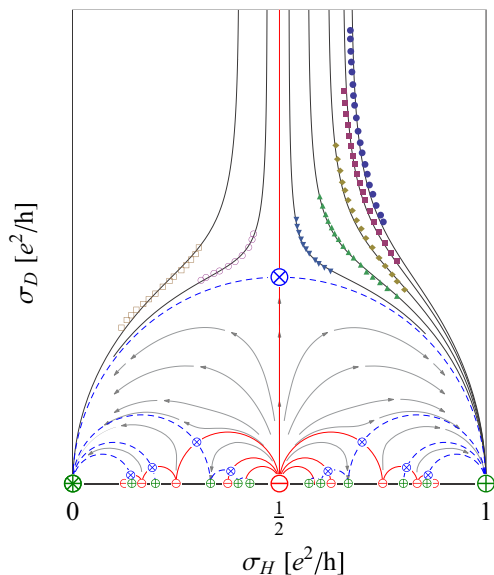


FIG. 10. Reconstruction of temperature-driven scaling data (discrete icons) exploring the plateau-insulator transition  $0 = \otimes \leftrightarrow \oplus = 1$  in a 2D ferromagnetic topological insulator [a thin film of  $\text{Cr}_x(\text{Bi}_{1-y}\text{Sb}_y)_{2-x}\text{Te}_3$  grown on a semi-insulating InP(111) substrate] [46].

Figure 11 shows our reconstruction of temperature-driven scaling data (discrete icons) exploring the plateau transitions  $1 \leftrightarrow 2 \leftrightarrow 3$  in a heterostructure  $\text{Hg}_x\text{Cd}_{1-x}\text{Te}/\text{HgTe}/\text{Hg}_x\text{Cd}_{1-x}\text{Te}$  ( $x \approx 0.7$ ) with a 20.3-nm-wide HgTe quantum well [51]. Since this thickness is well above  $d_c$ , there should be no Dirac cones in the bulk Brillouin zone. The sample was grown by molecular beam epitaxy on a GaAs substrate, symmetrically modulation doped with In at both sides of the quantum well, yielding a mobility of  $22 \times 10^4 \text{ cm}^2 \text{ V}^{-2} \text{ s}^{-2}$  and an electron gas density of about  $1.5 \times 10^{15} \text{ m}^{-2}$  [50,51].

The longitudinal and Hall resistivities were measured with a constant 1 A current in the temperature range 2.9–50 K, and a magnetic field strength in the 0–9 T range. There is clear evidence for plateaux at  $\nu = 1, 2, 3$ , and 4, obtained for magnetic fields in the range 1.8–8 T. For most magnetic field values the system exhibited scaling behavior for the five lowest temper-

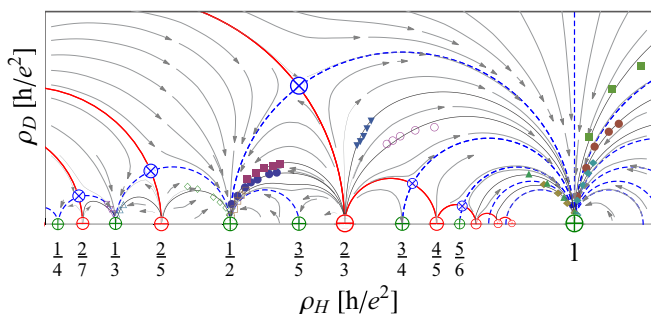


FIG. 11. Reconstruction of temperature-driven scaling data (discrete icons) exploring the plateau transitions  $1 \leftrightarrow 2 \leftrightarrow 3$  in a  $\text{HgTe}/\text{HgCdTe}$  heterostructure with a wide HgTe quantum well [51].

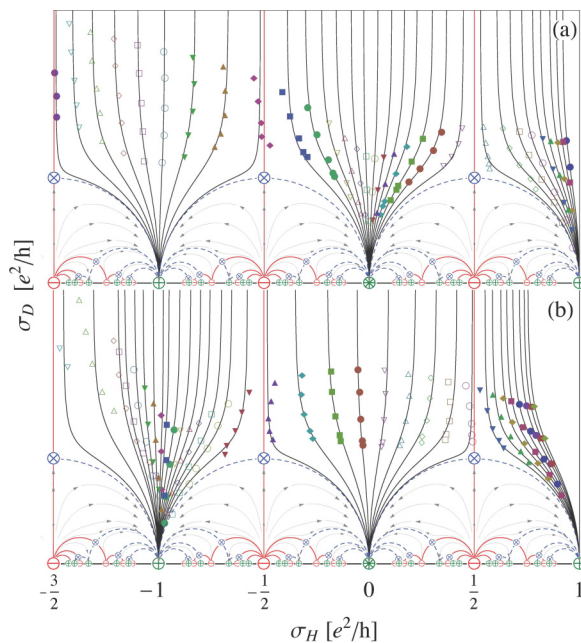


FIG. 12. Reconstruction of temperature-driven scaling data (discrete icons) exploring the plateau-insulator transitions  $-1 = \oplus \leftrightarrow \otimes \leftrightarrow \oplus = 1$  in a bismuth antimonide topological insulator ( $\text{Bi}_{1-x}\text{Sb}_x$ ) $_2\text{Te}_3$ , with (a)  $x = 0.88$  and (b)  $0.84$  [52].

atures  $T = 2.9, 4.1, 6.1, 8.1$ , and  $10$  K, and in one instance also for  $15$  and  $20$  K. In some cases, close to the fix points only the three lowest temperatures were usable. Comparison with a modular scaling flow (solid lines) with quantum critical points at  $\otimes = (2n + 1 + i)/(2n^2 + 2n + 1) = 1 + i, (3 + i)/5, (5 + 1)/13, (7 + i)/25, \dots$  reveals a  $\Gamma_T$  symmetry in the transport data (cf. Table I and Fig. 2).

### E. Plateau-insulator transitions in bismuth antimonide

In Ref. [52], the QHE was studied by measuring surface conductivities on the top and bottom of the three-dimensional topological insulator bismuth antimonide. Two 8-nm-thick TI films of  $(\text{Bi}_{1-x}\text{Sb}_x)_2\text{Te}_3$  ( $x = 0.84, 0.88$ ) were grown on insulating InP (111) substrates using molecular beam epitaxy. Quantum Hall signatures were found at magnetic field strengths above 14 T, for temperatures ranging from 700 mK down to 40 mK, at various gate voltages  $V_G$ .

Figure 12 shows our reconstruction of their temperature-driven scaling data (discrete icons) exploring the two plateau-insulator transitions  $-1 = \oplus \leftrightarrow \otimes \leftrightarrow \oplus = 1$ . Inaccessible data points and clear statistical outliers were not considered when sampling the data. Comparison with a modular scaling flow (solid curves) with quantum critical points at  $\otimes = (\pm 1 + i)/2, (\pm 3 + i)/2, \dots$  reveals a  $\Gamma_T$  symmetry in the transport data (cf. Table I and Fig. 2).

### F. Plateaux transitions in black phosphorus

In addition to graphene, black phosphorus is the only other 2D atomic crystal where a QHE has been observed. Figure 13 shows a scaling flow derived from our reconstruction of data obtained in an experiment on a few layers of black phosphorus,

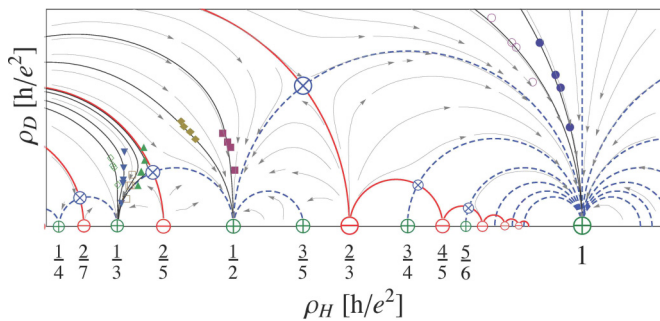


FIG. 13. Reconstruction of temperature-driven scaling data (discrete icons) exploring the plateau transitions  $1 \leftrightarrow 2 \leftrightarrow 3$  in black phosphorus [53].

which were sandwiched between two layers of insulating hexagonal boron nitride (hBN) and placed on a graphite backgate to create a van der Waals heterostructure [53].

The 25-nm bottom layer of hBN allows the electrons in the graphite to screen the impurity potential at the black phosphorus-hBN interface, which gives a record high Hall mobility of  $6000 \text{ cm}^2 \text{ V}^{-2} \text{ s}^{-2}$  for this material. It is this large mobility that gives an observable QHE [53].

The data are extracted from Fig. 7 of the supplementary material of Ref. [53]. The Hall resistances were measured at fixed magnetic fields of 27, 29, 31, and 33 T, and temperatures 1.7, 4.1, 4.6, 6, 8, and 10 K, by varying the back gate voltage from  $-2$  to  $-0.7$  V. Plateaux were discovered for filling factors  $\nu = 1, 2$ , and  $3$ . Due to overlap of the Hall resistance curves, an area of  $\sim \pm 013$  V at the inflection point of the  $1 \leftrightarrow 2$  transition had to be excluded. The curves for 8 and 10 K were also excluded because the magnetoresistance did not vanish on the plateaux.

Deriving the magnetoresistivity  $\rho_D = \lambda R_D$  from the measured magnetoresistance  $R_D$  requires knowing the aspect ratio  $\lambda = L_y/L_x$  of the Hall bar (of length  $L_x$  and width  $L_y$ ). Since this information was not provided in Ref. [53] we also fitted  $\lambda$ . The best fit of the data gave  $\lambda \approx 3$ , which is consistent with the optical image of the device (black phosphorus/hBN/graphite heterostructure) shown in Fig. 1(a) of Ref. [53]. Comparison with a modular scaling flow (solid lines) with quantum critical points at  $\otimes = (2n + 1 + i)/(2n^2 + 2n + 1) = 1 + i, (3 + i)/5, (5 + 1)/13, (7 + i)/25, \dots$  reveals a  $\Gamma_T$  symmetry in the transport data (cf. Fig. 2).

## V. UNIVERSALITY CLASS $\Gamma_R$

### A. Plateau-insulator transition in GaAs/GaAlAs

Figure 14 shows our reconstruction of temperature-driven scaling data (discrete icons) exploring the plateau-insulator transition  $0 \leftrightarrow 2$  in a GaAs/GaAlAs heterojunction [54]. Comparison with a modular scaling flow (solid lines) with a quantum critical point at  $\otimes = 1 + i$  reveals a  $\Gamma_R$  symmetry in the transport data (cf. Fig. 2).

### B. Plateau-insulator transition in graphene

Figure 15 shows our reconstruction of temperature-driven scaling data (discrete icons) exploring the plateau-insulator

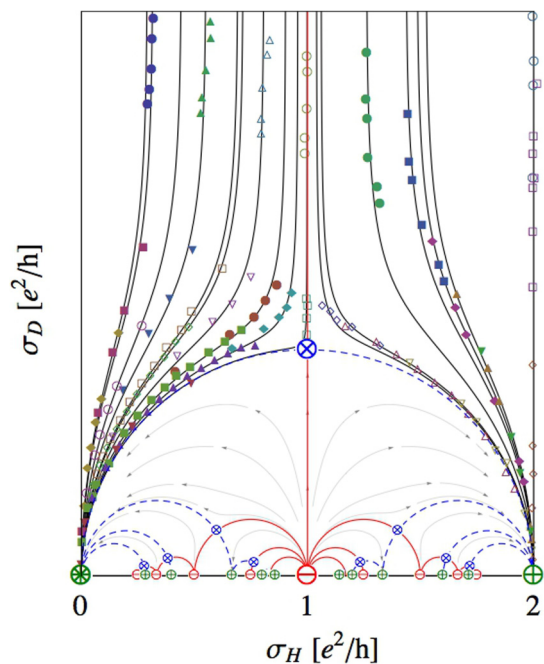


FIG. 14. Reconstruction of temperature-driven scaling data (discrete icons) exploring the plateau-insulator transition  $0 \leftrightarrow 2$  in a GaAs/GaAlAs heterojunction [54].

transition  $0 \leftrightarrow 2$  in graphene [55]. In order to compensate for what is presumably a systematic error of unknown origin, the dataset close to the dashed blue semicircle has been shifted up slightly, so that the flow does not violate the semicircle law (i.e., so that the flow does not cross the separatrix

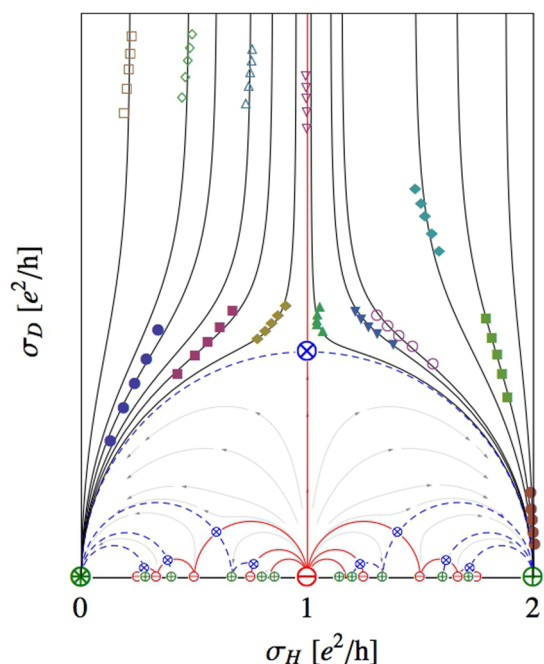


FIG. 15. Reconstruction of temperature-driven scaling data (discrete icons) exploring the plateau-insulator transition  $0 \leftrightarrow 2$  in graphene [55].

connecting the plateau  $\oplus$  to the insulator  $\otimes$  via the critical point  $\otimes$ . Comparison with a modular scaling flow (solid lines) with a quantum critical point at  $\otimes = 1 + i$  reveals a  $\Gamma_R$  symmetry in the transport data (cf. Fig. 2).

In this experiment, large-area ( $0.6 \times 0.1 \text{ mm}^2$ ) monolayer graphene devices were made by epitaxial growth on SiC-substrate. In the devices, a buffer layer of graphene made partial covalent bonds with the exposed Si atoms and only the top graphene layer was conducting. Experiments were made in the temperature range 2.6–25 K with magnetic fields in the range 0.1–9 T.

According to Ref. [55] the graphene-substrate coupling, which includes Si-C covalent bonds and defects, such as interfacial dangling bonds, can be strong enough to break the sublattice symmetry of the conducting graphene sheet. In order to enhance this effect, the Coulomb screening of potential fluctuations was reduced by engineering the carrier density to be as low as  $n \approx 10^{15} \text{ m}^{-2}$ . This may be the reason for the appearance of an insulator phase, which signals that the  $\Gamma_Q$  symmetry observed in ordinary monolayer graphene has been transmuted to a  $\Gamma_R$  symmetry (cf. Fig. 5).

The data that best fit the flow lines are taken from one of the least disordered samples which also had the highest surface roughness (called EG2 in Ref. [55]). The data from the other sample (EG3) appears to fit slightly better if shifted up by about  $0.03e^2/h$ . This may be the result of a small systematic error, but it is so small that it may be within the random error of this experiment.

## VI. UNIVERSALITY CLASS $\Gamma_Q$

We have already mentioned the spectrum of plateaux observed in some experiments on graphene. The competition between several scales is not easy to disentangle, especially in crossover regions where the lowest Landau level may be more susceptible to symmetry breaking than higher levels. However, so far, it seems that the symmetries we have discussed (cf. Fig. 1) suffice to account for the plateaux data.

A much more stringent test is, as we have seen in the nonrelativistic case, to compare the unstable fixed points with experimental quantum critical points. Scaling experiments on graphene are still in their infancy, and the paucity of data means that this analysis is far from conclusive. Unfortunately, so far, a meaningful comparison is only possible for the doubly degenerate IQHE, which should be compared with the phase and flow diagram in Fig. 2.

Because of the zero mode there is no QHI ( $\sigma_{\oplus} = \otimes = 0$ ) in this case, so  $\Gamma_T$  and  $\Gamma_R$  are immediately eliminated as potential symmetries. A glance at the defining characteristics of the groups in Eq. (1) shows that, up to a factor of two,  $\Gamma_S$  is the only viable candidate. Because of the double degeneracy in graphene the conductivity should be doubled [56],  $\sigma \rightarrow 2\sigma = G(\sigma)$ , giving the  $\Gamma_Q$ -symmetric phase and flow diagram shown in the bottom panel of Fig. 2.

An immediate consequence is that fractional plateaux in the doubly degenerate QHE should appear only at  $\sigma_H = 2(2n + 1)/(2m + 1) \not\equiv \pm 1/3$ . In fact,  $\sigma_H = 1/3$  has also been observed, but only when the magnetic field is so strong that one expects the spin-valley degeneracy to be lifted, which transmutes  $\Gamma_Q$  to  $\Gamma_R$  or  $\Gamma_T$ .

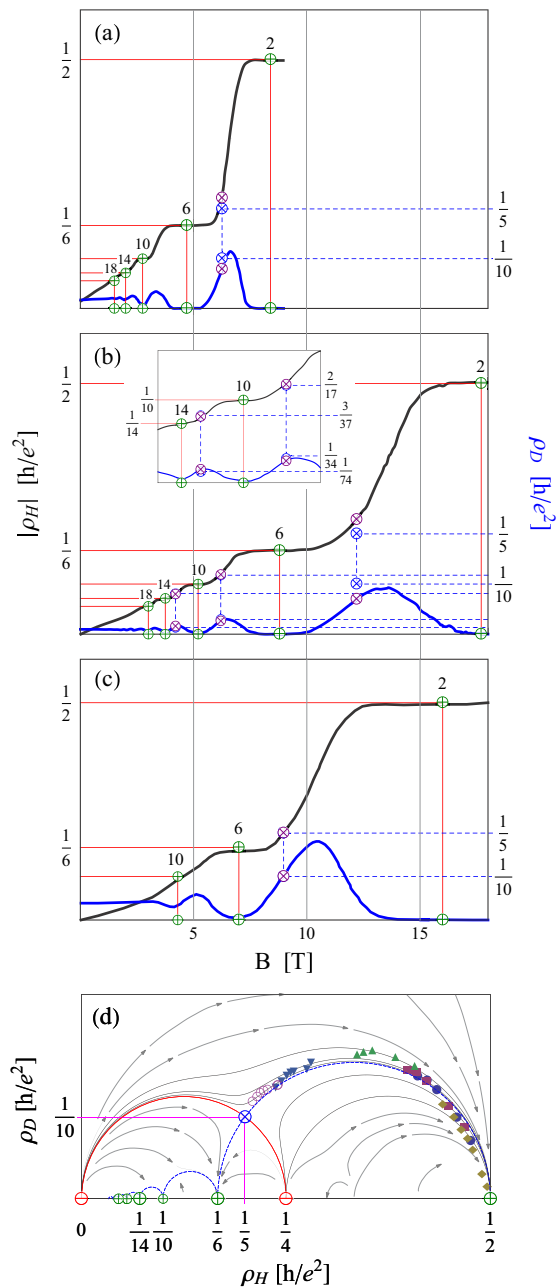


FIG. 16. (a)–(c) Experimental quantum Hall data for graphene reconstructed from [57–59], compared with modular critical points (blue  $\otimes$ ). (d) Scaling flow derived from reconstructed graphene data published in Ref. [59], superimposed on the phase diagram with  $\Gamma_Q$  symmetry (cf. Fig. 2).

### A. IQHE in graphene

Figure 16 is a reconstruction of some experimental quantum Hall data for graphene [57–59], compared with modular critical points (blue  $\otimes$ ). As explained in Sec. II, ideally we would like to have a family of scaling data deep inside the scaling domain, in which case we could obtain the experimental critical point from the temperature independent crossing point of the curves. Unfortunately, such data are still not available for graphene. The family of data published recently are consistent with our estimate, but not good enough to resolve any discrepancy in

detail [59]. This is why only the data obtained at the lowest temperature (4.1 K) has been used in Fig. 16(c).

In lieu of such “family portraits,” we use the translational symmetry in the conductivity of the IQHE to estimate the location of experimental critical points. If we are close enough to the scaling domain critical points should lie at the apex of the arcs in the conductivity graph connecting neighboring plateaux, i.e., where the experimental conductivity graph crosses the vertical lines  $\sigma_H = 4n$  (cf. Fig. 2). Mapping these points back onto the resistivity data gives the experimental critical points  $\otimes$  (purple icons) shown in Fig. 16, which mostly eclipse the modular predictions  $\oplus$  (blue icons).

Figure 16(a) is our reconstruction of the first data on the  $2 \leftrightarrow 6$  transition, discovered in 2005 [57,60]. Figure 16(b) shows the  $2 \leftrightarrow 6 \leftrightarrow 10 \leftrightarrow 14$  transitions explored in 2009 [58]. The latter two transitions are magnified in the inset, but the distinction between experimental and  $\Gamma_Q$  critical points is still not resolved in this plot. Figure 16(c) shows more recent data on the  $2 \leftrightarrow 6 \leftrightarrow 10$  transitions [59]. In this case, the fixed point of  $\Gamma_Q$  is totally eclipsed by the experimental critical point. In all cases, the overlap of experiment and theory is reasonable, and possibly within experimental error, although no error analysis of these experiments has been published. Figure 16(d) shows a scaling flow derived from reconstructed graphene data published in [59], superimposed on the phase diagram with  $\Gamma_Q$  symmetry (cf. Fig. 2).

We see that it is possible that the earliest graphene experiments [Figs. 16(a) and 16(b)] had not yet reached the scaling limit, which is where an approximate low-energy symmetry would appear. The good agreement with the most recent data in Fig. 16(c) notwithstanding, since these experiments have only probed the IQHE in graphene, it is premature to claim that these experiments unambiguously demonstrate the emergence of a modular symmetry in this material. This question can only be settled by more accurate scaling experiments involving transitions to fractional plateaux.

### B. FQHE in graphene

Since they were discovered in 2009 many fractional plateaux have been found in graphene [62,63]. A recent study found some intriguing new fractional plateaux in graphene [64]:

$$\sigma_H = \begin{cases} \frac{1}{3}, \frac{2}{3}, \frac{2}{5}, \frac{3}{5}, \frac{3}{7}, \frac{4}{7}, \frac{4}{9} & \text{for } 0 < \nu < 1, \\ \frac{4}{3}, \frac{8}{5}, \frac{10}{7}, \frac{14}{9} & \text{for } 1 < \nu. \end{cases}$$

The first sequence is consistent with  $\Gamma_T$ , in which case both the spin and pseudospin has been resolved. Barring coincidences, the second sequence appears to be constrained to have only even numerators. Since  $4/3, 8/5 \notin \oplus_Q$ , the only possibility appears to be  $\Gamma_R$ , which has plateaux

$$\oplus_R = \frac{2n}{2m+1} \ni \frac{4}{3}, \frac{8}{5}, \frac{10}{7}, \frac{14}{9}, \dots$$

A possible interpretation is that either the spin or the pseudospin degeneracy has been fully resolved, while the other remains at least partially degenerate (cf. Fig. 5). This is consistent with the expectation that the lowest level will be most susceptible to symmetry-breaking (cf. Fig. 20).

## VII. TRANSMUTATIONS

When one or more control parameter of an experiment changes, an external electric field, say, a modular symmetry can be transmogrified into another modular symmetry. This “morphing” may be a consequence of some discrete microscopic symmetry being broken, but unless the new modular group is a subgroup of the original group, we will call this a *crossover* or *transmutation*, rather than *symmetry breaking*. We discuss some examples of this that have been explored experimentally.

### A. $\Gamma_R \rightarrow \Gamma_T$

We turn now to some experiments that have explored the transition from nonrelativistic degenerate (unpolarized) to nondegenerate (fully polarized/spin split) bands, by tuning the spin splitting using a backgate voltage. By the arguments discussed in the first section, we expect these data to interpolate between the two maximal submodular symmetries  $\Gamma_R$  (unpolarized) and  $\Gamma_T$  (polarized). When the Zeeman splitting is between these extremes the modular symmetry must be at least partially broken, but possibly only to their maximal common subgroup  $\Gamma(2)$  (cf. Fig. 1).

The panels inside the box on the right hand side of Fig. 17 shows a reconstruction of temperature-driven scaling data (discrete icons) exploring the transitions  $0 = \otimes \leftrightarrow \oplus = 1 \leftrightarrow \oplus = 2$  in GaAs with self-assembled InAs dots [61]. The transition from degenerate (unpolarized) to nondegenerate (fully polarized/spin split) bands is explored by tuning the spin-orbit interaction using a backgate voltage, and compared to the family of physically viable  $\Gamma(2)_2$ -invariant RG potentials (cf. Sec. II)  $\varphi_a \propto \ln \lambda + (a-1) \ln(\lambda-1)$  [22], with values of the real parameter  $a$  ranging from  $a_R = -1$  to  $a_T = 1/2$  in this experiment. All solid lines are flow trajectories derived by numerical integration from the gradient flow generated by this potential. For clarity, we display only those parts of the modular phase boundaries (red curtains) that are above all separatrices (blue canopies).

By comparing the data for the  $0 \leftrightarrow 1$  transition with the flow derived from  $\varphi_{1/2}$  (left front panel), we see that the scaling flow in this case appears to respect  $\Gamma_T$  symmetry. This is not so for the  $1 \leftrightarrow 2$  transition (right front panel, reconstructed from Fig. 2(c) in [61]), which we have included for completeness. Several of the experimental flow lines cross the separatrix (dashed blue semicircle). This is a rare example where the  $\Gamma(2)_2$  symmetry appears to be broken, but this may simply be because the experiment did not reach the scaling domain. Indeed, a closer inspection of the experimental data (cf. Fig. 8 in Ref. [61]) reveals that only for a couple of the lowest temperatures are the plateaux well developed. We should therefore not expect a flow derived from the full set of data to respect any modular symmetry, since they are not proper scaling data.

It is instructive to examine these flows in more detail, compare panels on the left-hand side of Fig. 17, which also includes some other experiments that were discussed in Ref. [22]. This reconstruction of temperature-driven scaling data (discrete icons) is derived from a wide range of different 2D materials, and explores various parts of the landscape of

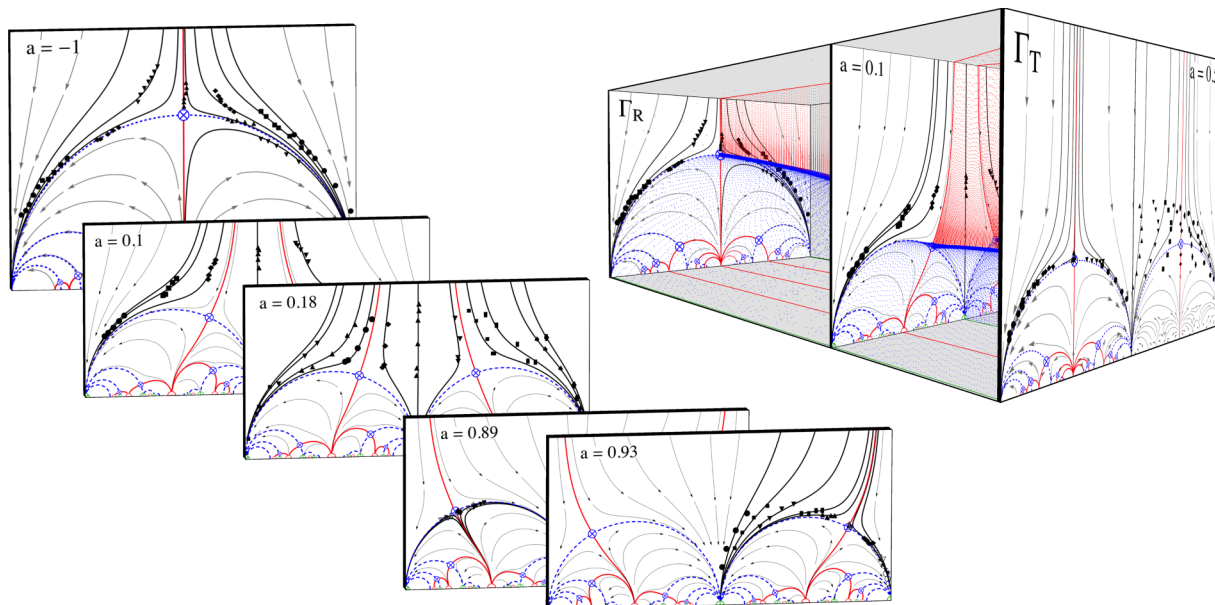


FIG. 17. (Left) Reconstruction of temperature-driven scaling data (discrete icons) exploring various parts of the landscape of  $\Gamma(2)$ -symmetric scaling flows in  $\sigma(t)$ , derived from a wide range of different 2D materials (cf. Fig. 4) [61]. (Right) Reconstruction of temperature-driven scaling data (discrete icons) exploring the transitions  $0 = \otimes \leftrightarrow \oplus = 1 \leftrightarrow \oplus = 2$  in GaAs with self-assembled InAs dots, for various values of the spin splitting (parametrized by  $a$ ), which was tuned using a backgate voltage [61].

$\Gamma(2)$ -symmetric scaling flows. As in all our diagrams, solid lines are flow trajectories derived by numerical integration from the gradient flow generated by the RG potential  $\varphi_a$ .

It is interesting to note the severe deformation of the fractional phases when the symmetry is broken to  $\Gamma(2)$ . This is a consequence of the dramatic transmogrification that must take place in passing from one subfamily to another (cf. Figs. 3 and 4). When fractional quantum Hall data become available for these and similar materials, these predictions will provide a very stringent test of modular symmetry.

### B. $\Gamma_Q \rightarrow \Gamma_R$

Figure 18 illustrates a conjectured modular explanation of a peculiar phenomenon observed in a graphene device [65]. This experiment appears to show that an insulator phase can inject itself into the standard graphene sequence  $\dots - 6 \leftrightarrow - 2 \leftrightarrow 2 \leftrightarrow 6 \dots$ , giving  $\dots - 6 \leftrightarrow - 2 \leftrightarrow \otimes \leftrightarrow 2 \leftrightarrow 6 \dots$ , without being accompanied by other new plateaux. This would mean that the modular symmetry is completely broken.

If a modular symmetry is still at large, then the appearance of an insulator phase at  $\oplus = \otimes = 0$  could mean that the original symmetry  $\Gamma_Q$  has been transmuted into  $\Gamma_R$  or  $\Gamma_T$  (cf. Fig. 2). Since five of the six peaks in  $\sigma_D$  have roughly the same height  $\max(\sigma_D) \approx 1 [e^2/h]$  (cf. inset in Fig. 18), the leading candidate is  $\Gamma_R$ :

$$\otimes_Q = 4n + 2i \xrightarrow{\text{"split"}} \otimes_R = 1 + 2n + i \quad (n \in \mathbb{Z}).$$

If so, there should be structure emerging in the  $-2 \leftrightarrow 2$  and  $\pm 2 \leftrightarrow \pm 6 \leftrightarrow \pm 10 \dots$  transitions, signaling that new plateaux are germinating at  $\oplus = 0 \pmod{4}$ . In this experiment,

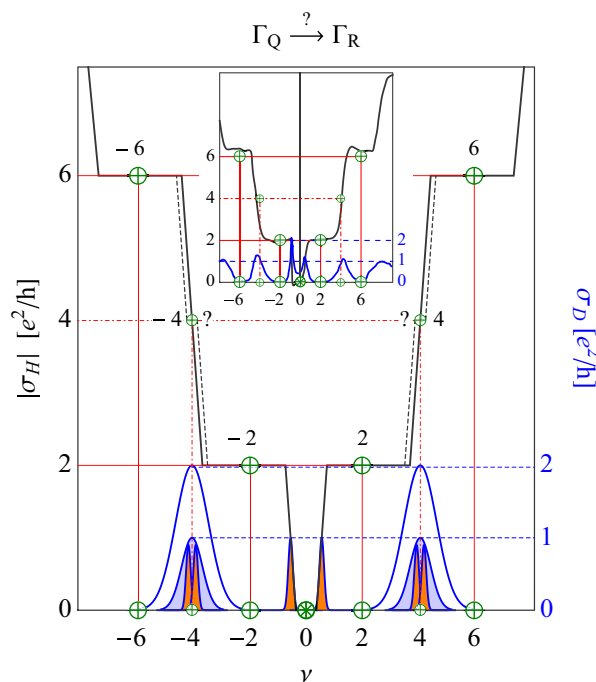


FIG. 18. Schematic diagram of conductivity data (reconstructed in the inset) as a function of the filling factor  $\nu = n_s h/eB$  ( $B = 18$  T,  $T = 250$  mK), from an experiment that perhaps may be interpreted as probing the crossover  $\Gamma_Q \rightarrow (\Gamma_R) \rightarrow \Gamma_T$  in a graphene sample (cf. Fig. 5) [65]. The diagram illustrates how a suppression of a peak in  $\sigma_D$  may be the first sign that a new phase is germinating, before the new plateau in  $\sigma_H$  or the associated splitting of  $\sigma_D$  can be experimentally resolved. If the magnetic field strength is increased further, we expect the band structure to eventually be fully resolved (spin-valley splitting), and a second transmutation  $\Gamma_R \rightarrow \Gamma_T$  would suppress the peaks further,  $\sigma_D \rightarrow 1/2$ .

we see two new peaks in  $\sigma_D$  developing near the new plateau at  $\oplus = \otimes = 0$ , as expected, but no other new plateaux in  $\sigma_H$  are resolved, and the original peaks in  $\sigma_D$  are suppressed rather than split.

A possible explanation is that even if both the new plateaux and the new zeros in  $\sigma_D$  are insufficiently developed to be resolved by this experiment, the new zeros in  $\sigma_D$  that eventually develop at  $\oplus = \pm 4, \pm 8, \dots$  may be forcing an observable suppression of the peaks of  $\sigma_D$ . In other words, when a critical point “splits” in order to make room for a new phase, the presence of this new pair of critical points could at first appear as a suppression of the original peak, as is seen in this experiment. When the plateau is fully developed there should be two peaks instead of one, both smaller than the original peak (cf. Fig. 2), as seen for the insulator transitions in Fig. 18.

In this experiment, when the insulator phase is present the height of all but one of the peaks in  $\sigma_D$  is consistent with  $\Gamma_R$  symmetry (cf. inset in Fig. 18). This does not explain why the remaining peak is twice as large, but the asymmetry in the data, as well as the crude Hall quantization that only roughly approximates the expected integers ( $\oplus = 2 \pmod 4$ ), suggests that there are large systematic errors of unknown origin that may be responsible for skewing the data.

### C. $\Gamma_Q \rightarrow \Gamma_T$

The valley degeneracy in graphene is protected by an inversion symmetry of the carbon lattice. It seems to be very difficult to lift some or all of this degeneracy without also destroying the Dirac cones, and the transmutation  $\Gamma_Q \rightarrow \Gamma_S$  has not been seen (cf. Fig. 5). We consider first the simplest case where both spin and valley symmetry is broken by a very strong magnetic field, which gives the transmutation  $\Gamma_Q \rightarrow \Gamma_T$ .

Figure 19 shows a reconstruction of resistivity data from a pair of graphene experiments that appear to be showing the crossover  $\Gamma_Q \rightarrow \Gamma_T$  (cf. Fig. 5) [36,57]. In both experiments the density of states was controlled by a backgate potential  $|V_g| < 80$  V, in a fixed background magnetic field  $B$  and constant temperature  $T$ .

With  $B = 9$  T and  $T = 1.6$  K at least fourteen plateaux at  $\sigma_{\oplus} = 4n + 2$  ( $n = -7, -6, \dots, 5, 6$ ) were observed, cf. Fig. 19(a), but no insulator phase [57]. This is consistent with  $\Gamma_Q$  symmetry. The dotted blue lines connected to the stack of unstable fixed points ( $\ominus \leftarrow \otimes \rightarrow \ominus$ ) is a visual mnemonic to remind us of the modular quantum critical point expected to appear at  $\rho_{\otimes} = i/2 [h/e^2]$ , which was not accessible in this experiment.

In a much stronger magnetic field  $B = 45$  T, and similar temperature  $T = 1.4$  K, the double spin-valley degeneracy appears to be completely broken, cf. Fig. 19(b). In addition to the weak field plateaux [Fig. 19(a)], new plateaux were observed at  $\sigma_{\oplus} = 0, \pm 1, \pm 4 [e^2/h]$ , and  $\rho_D$  is showing preliminary signs (splitting and suppression) of additional plateaux germinating at  $\sigma_{\oplus} = \pm 3 [e^2/h]$ , and perhaps also at  $\sigma_{\oplus} = \pm 5 [e^2/h]$  [57]. This is consistent with the  $\Gamma_T$  symmetry expected when both the spin and pseudospin degeneracies have been resolved. The dotted lines connecting some plateaux to the insulator fixed point  $\rho_{\otimes} = i\infty$  is a reminder that modular symmetry does not predict a quantized value of the Hall potential in this phase ( $\rho_H \in \mathbb{R}$ ). Equivalently, both the Hall

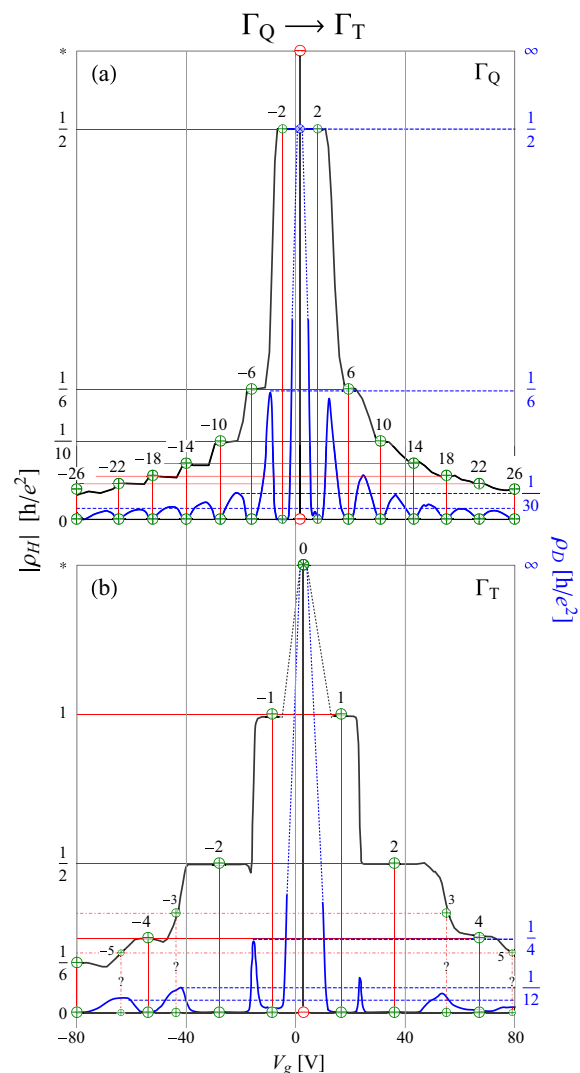


FIG. 19. Reconstruction of resistivity data (solid curves) from two graphene experiments in a constant external magnetic field. Both the plateaux spectrum and relative heights of the peaks in the magnetoresistivity  $\rho_D$ , (a) in a “weak” field  $B = 9$  T [57], and (b) in a strong field  $B = 45$  T [36], is consistent with the transmutation  $\Gamma_Q \rightarrow \Gamma_T$  of modular symmetry (cf. Fig. 5).

and magnetoconductivities vanish at the IR fixed point  $\sigma_{\otimes} = 0$  on the boundary of this phase (yellow region in Fig. 2).

In the absence of sufficient information about the geometry of these Hall devices, we have in both diagrams chosen to normalize the magnetoresistance  $\rho_D$  so that the principal left peak takes the maximum value expected from modular symmetry (i.e., the height of the relevant semicircular separatrix, compare top and bottom right panels in Fig. 2). In both cases, the subleading left peak [and in (b) also the next peak to the left] are in reasonable agreement with the expected (maximal) modular values of  $\rho_D$ , indicated here by dashed blue lines. There is, however, a substantial asymmetry between the data on the right and left hand side, which is not expected if the emergent symmetry is fully developed.

Figure 20 shows a schematic illustration of a conjectured band structure as a function of an external magnetic field strength  $B$ , inferred from graphene data obtained at  $T = 1.4$  K



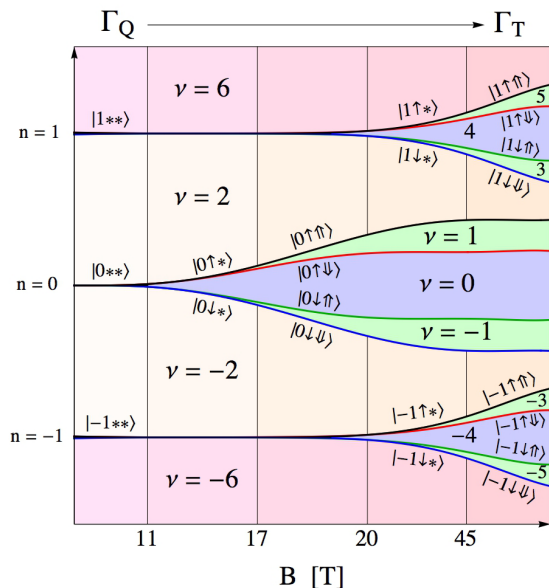


FIG. 20. Schematic illustration of conjectured band structure of a graphene sample investigated at  $T = 1.4$  K as a function of an external magnetic field strength  $B < 45$  T [66]. Colored regions labeled by filling factors  $\nu$  are gaps between the bands, which are represented here by curves labeled with spin-up state vectors  $|n; \uparrow\rangle$  (black) and  $|n; \uparrow\rangle$  (red), and spin-down states  $|n; \downarrow\rangle$  (green) and  $|n; \downarrow\rangle$  (blue), for the three Landau levels  $n = 0, \pm 1$ . The high and low field limits are consistent with, respectively,  $\Gamma_T$  and  $\Gamma_Q$ .

with  $B < 45$  T [66]. Each time a band splits, a new delocalized state appears, giving rise to an additional plateau in the Hall conductivity. Splitting spin states  $|n; \uparrow, * \rangle$  and  $|n; \downarrow, * \rangle$  gives a blue gap, while splitting valley states  $|n; *, \uparrow \rangle$  and  $|n; *, \downarrow \rangle$  gives a green gap. Gaps are uniquely labeled by the filling factor  $\nu$ .

The weak (left) and strong (right) field limits are consistent with the transmutation  $\Gamma_Q \rightarrow \Gamma_T$  of modular symmetry (cf. Fig. 5). However, if the degeneracy in the lowest Landau level is less robust than for higher levels, so that the splitting happens at different values of the magnetic field  $B$ , then at intermediate values of  $B$  neither symmetry will be manifest in the spectrum of plateaux.

Tilted field data obtained in this experiments [66] seems to show that spin splitting is easier to achieve than valley splitting in graphene, at least for the lowest Landau levels, so that there is a hierarchy in the spin-valley splitting sequence for increasing values of the external magnetic field (cf. Fig. 20) ( $[B] = T$ ):

$$\begin{aligned}
 \oplus_{\mathbb{Q}} & \xrightarrow{B < 11} \pm 2 \leftrightarrow \pm 6 \leftrightarrow \pm 10 \dots \xrightarrow{B > 11} \\
 0 & \xrightarrow{B > 17} \pm 2 \leftrightarrow \pm 6 \leftrightarrow \pm 10 \dots \xrightarrow{B > 20} \\
 0 & \xrightarrow{B > 20} \pm 1 \leftrightarrow \pm 2 \leftrightarrow \pm 6 \leftrightarrow \pm 10 \dots \xrightarrow{B > 45} \\
 0 & \xrightarrow{B > 45} \pm 1 \leftrightarrow \pm 2 \leftrightarrow \pm 4 \leftrightarrow \pm 6 \leftrightarrow \pm 10 \dots \xrightarrow{B \rightarrow \infty} \\
 \dots & \dots \dots \dots \\
 0 & \xrightarrow{B \rightarrow \infty} \pm 1 \leftrightarrow \pm 2 \leftrightarrow \pm 3 \leftrightarrow \pm 4 \leftrightarrow \pm 5 \dots = \oplus_{\mathbb{T}},
 \end{aligned}$$

where we have allowed for the possibility (not shown in Fig. 20) that there are additional levels in the hierarchy if higher Landau levels are not equally robust.

Since the valley degeneracy is protected by inversion symmetry of the graphene lattice, which is not broken by the external field, the valley splitting presumably depends on the subtle energetics of many-body interactions in this material. A detailed understanding of this hierarchy is therefore a difficult dynamical problem that is only tractable in limiting cases (e.g.,  $0 \leftarrow B \rightarrow \infty$ ), where the identification of emergent modular symmetries may be useful.

## VIII. DISCUSSION

We have reviewed experimental quantum Hall scaling data from a wide selection of materials, and compared these with modular flow diagrams derived from the *holomorphic Hall potential*  $\varphi_a = \ln \lambda + (a - 1) \ln(\lambda - 1)$  that is parametrized by a single real number  $a$  [22]. This potential is invariant under the congruence subgroup  $\Gamma(2)$  of the full modular group  $SL(2, \mathbb{Z})$ , because it is built only from the classical *elliptic modular lambda function*  $\lambda$  [67].

In Secs. I and II, we have explained and emphasized that the physical properties that must be required of any  $\Gamma(2)$ -invariant scaling function  $\beta_a = \partial \varphi_a$  renders the functional form of the RG potential  $\varphi_a$  essentially unique (up to normalization). The key is to recognize the holomorphic modular structure of the parameter space, which must be respected by the scaling functions. It is the pincer movement of a complex structure and modular symmetry that pins down the RG potential [68].

For  $a = -1, 1/2$ , and  $2$ , the symmetry is enhanced to the maximal subgroups  $\Gamma_R, \Gamma_T$  and  $\Gamma_S$ , respectively. So, if the emergent symmetry is observed to be  $\Gamma_X$  ( $X = Q, R, S, T$ ), then the  $\beta$  function, and therefore the phase and flow diagram, is *unique* (up to normalization). Since these are the symmetries that are most often encountered in the QHE, it is easy to falsify the modular hypothesis (i.e., the relevance of  $\varphi_a$  for the QHE), but this is not what has happened. As technology has improved over the past three decades, so has the agreement between experimental scaling data and modularity. Compare, for example, our reconstruction of data from 1985 shown in Fig. 6 with Fig. 10 (data from 2014) or Fig. 12 (data from 2015).

In addition to the fact that some of the modular predictions from 1992 have been verified at the *per mille* level [1, 2, 20, 24], it is perhaps the overall agreement of the unique modular family of level two flow diagrams with a wide range of different materials and experimental circumstances that is the most convincing evidence for “modular universality” in the QHE.

There have been various attempts over the years to analyze the phase structure of the QHE, starting with a proposal based on the translation symmetry of RG flows in the IQHE [69]. This was motivated by a sigma-model of localization [27, 70–76], but the target space geometry does not appear to be rich enough to include the FQHE.

In Refs. [1, 2], it was proposed that a modular symmetry would be capable of describing both the integer and the fractional Hall effects, by including dualities in addition to translations, as described in the introduction. The three maximal subgroups  $\Gamma_R, \Gamma_S$ , and  $\Gamma_T$  were immediately identified as the

largest symmetries of physical interest.  $\Gamma_T$  was shown to give the correct phenomenology for the spin-polarized QHE,  $\Gamma_S$  was proposed as the relevant symmetry for analogous transport problems with bosonic quasiparticles, and the symmetry  $\Gamma(2)$  and the idea of a potential interpolating between the enhanced symmetries was introduced [4].

At roughly the same time superficially similar dualities acting on the filling fraction  $\nu$  were considered [77–82], and the resulting transformations are known collectively as “the law of corresponding states.” Since  $\nu$  is essentially the plateau value  $\sigma_{\oplus} = \sigma_H \in \mathbb{R}$ , this approach is oblivious to the complex structure that gives modular symmetry most of its predictive power. These dualities appear to disagree with experiment, unlike the complexified duality identified in Refs. [1,2], which is in excellent agreement with available data [17,19,20,24].

There have been two other attempts to construct families of interpolating  $\beta$  functions for the QHE [5,6,9–11,14,21]. They have both retained the original idea that the  $\beta$  function should be a modular form of weight two [1,2,7,8,15], and their work looks superficially similar to ours. This is because a flow line derived from *any* function with maximal modular symmetry always has the same shape, so plots of the vector fields will appear to be identical. As was explained in Refs. [1–4] this is a mathematical trick, which we also employed in order to obtain the original phase diagrams, but by itself this is not sufficient to build a physical model. Subsequent alternative proposals did not heed this advice. They did not pay sufficient attention to the physical properties that critical points must have, nor did they consider the elementary but demanding experimental constraints on scaling that we discussed in the introduction. Consequently, the conjectured “ $\beta$  functions” are not well motivated, nor do they appear to have any reasonable physical interpretation, as we now explain.

An interpolating  $\beta$  function, which in our notation is  $\beta_{\tilde{a}} \propto (\tilde{a}\lambda - 1)/\theta_3^4$  was proposed in Refs. [5,6,9,14]. They conclude that the location of the zero of this function is not predicted by  $\Gamma(2)$  symmetry, which is correct since it depends on the free parameter  $\tilde{a}$ , similar to our  $a$ . However, they seem ambivalent about the order of the transition point, they do not consider the family of functions under deformations of  $\tilde{a}$ , and they do not discuss the points of enhanced symmetry.

A family of meromorphic functions that was conjectured to be an interpolating  $\beta$  function was postulated in Refs. [11,21]. However, these “scaling functions” have no physical foundation or interpretation. In particular, they have poles where there should be critical points, i.e., where a physical  $\beta$  function must vanish. Critical exponents are therefore ill defined, and there is no physical scaling.

These attempts to implement the modular ideas introduced in Refs. [1–4] have all failed for the same reason: they ignored the complex structure and physical requirements that the scaling function must respect, i.e., *the geometric structure of*

*the effective (emergent) theory*. This is in sharp contrast to the work discussed here. Since our  $\beta$  function is derived from a physically motivated and physically sensible potential, it is by construction well behaved everywhere on the interior of parameter space. This includes the critical points where it has simple zeros, and therefore well defined scaling and critical exponents. The reason that the “mock  $\beta$  functions” used in Refs. [1–4] turned out to be essentially the same as  $\partial\varphi_a$ , is that they are subjugated by the same holomorphic modular structure. Given this geometric structure, the fate of the model is sealed, and the modular predictions made in 1992 are either right or wrong, at least for the maximally symmetric cases that are most frequently encountered in experiments. Fortunately, as we have seen here, there is now a large and growing body of evidence in good agreement with many modular scaling predictions.

We have also discussed some experiments where the modular symmetry is transmuted or broken. We have described in detail the most benign scenario, where the symmetry is “morphing” between maximally symmetric cases, while maintaining a maximal amount of unbroken modular symmetry. This is captured by a unique interpolating family of scaling diagrams with minimal symmetry breaking. The simplest physical example is when cranking up the magnetic field changes an unpolarized (spin degenerate) QHE to a polarized QHE. This is consistent with some experiments, but in a few cases modular symmetry is more severely broken or hidden. It is an important outstanding problem to find out when and how this happens, not only to delineate the domain where emergent modular symmetries are relevant, but also in order to understand why they are so accurate when they do appear. In summary, all scaling properties of almost all quantum Hall systems seems to be encoded in the deceptively simple looking RG potential  $\varphi_a$  [22].

Perhaps the biggest outstanding problem in the QHE is to determine the value(s) of the critical (delocalization) exponent(s), which would completely nail down the quantum Hall universality class(es). This exponent is determined by the curvature of the RG potential at a critical point, and therefore depends on the normalization of the  $\beta$  function. This number does not follow from symmetry alone, and information about the dynamics of the collective (emergent) modes relevant at low energy is required. The Ising model provides a helpful analogy. Kramers and Wannier managed to calculate the exact value the critical temperature (location of the critical point) by exploiting a  $\mathbb{Z}_2$  duality that is similar to  $S$  duality acting on  $\sigma_D$ , but the exact value of the critical exponent remained beyond reach until Onsager solved the model completely. Similarly, modular symmetry is by itself not sufficient to find the low-energy effective field theory, but (unlike  $\mathbb{Z}_2$ ) because it is an infinite non-Abelian group, it does severely limit the supply of candidate models, and may therefore provide valuable assistance in the search for this theory.

- [1] C. A. Lütken and G. G. Ross, Duality in the quantum Hall system, *Phys. Rev. B* **45**, 11837 (1992).  
 [2] C. A. Lütken and G. G. Ross, Delocalization, duality, and scaling in the quantum Hall system, *Phys. Rev. B* **48**, 2500 (1993).

- [3] C. A. Lütken, Global phase diagrams for charge transport in two dimensions, *J. Phys. A: Math. Gen.* **26**, L811 (1993).  
 [4] C. A. Lütken, Geometry of renormalization group flows constrained by discrete global symmetries, *Nucl. Phys. B* **396**, 670 (1993).

- [5] Y. Georgelin and J. C. Wallet, Group  $\Gamma(2)$  and the fractional quantum Hall effect, *Phys. Lett. A* **224**, 303 (1997).
- [6] Y. Georgelin, T. Masson, and J. C. Wallet, Modular groups, visibility diagram and quantum Hall effect, *J. Phys. A: Math. Gen.* **30**, 5065 (1997).
- [7] C. P. Burgess and C. A. Lütken, One-dimensional flows in the quantum Hall system, *Nucl. Phys. B* **500**, 367 (1997).
- [8] C. P. Burgess and C. A. Lütken, On the implications of discrete symmetries for the  $\beta$ -function of quantum Hall systems, *Phys. Lett. B* **451**, 365 (1999).
- [9] Y. Georgelin, T. Masson, and J. C. Wallet,  $\Gamma(2)$  modular symmetry, renormalization group flow and the quantum Hall effect, *J. Phys. A: Math. Gen.* **33**, 39 (2000).
- [10] Y. Georgelin, T. Masson, and J. C. Wallet, Visibility diagrams and experimental stripe structures in the quantum Hall effect, *J. Phys. A: Math. Gen.* **33**, 8649 (2000).
- [11] B. P. Dolan, Duality in the quantum Hall effect: The role of electron spin, *Phys. Rev. B* **62**, 10278 (2000).
- [12] C. P. Burgess and B. P. Dolan, Particle-vortex duality and the modular group: Applications to the quantum Hall effect and other two-dimensional systems, *Phys. Rev. B* **63**, 155309 (2001).
- [13] C. P. Burgess and B. P. Dolan, Duality and nonlinear response for quantum Hall systems, *Phys. Rev. B* **65**, 155323 (2002).
- [14] F. Chandelier, Y. Georgelin, T. Masson, and J. C. Wallet, Global quantum Hall phase diagram from visibility diagrams, *Phys. Lett. A* **301**, 451 (2002).
- [15] C. A. Lütken, Holomorphic anomaly in the quantum Hall system, *Nucl. Phys. B* **759**, 343 (2006).
- [16] C. A. Lütken and G. G. Ross, Anti-holomorphic scaling in the quantum Hall system, *Phys. Lett. A* **356**, 382 (2006).
- [17] C. A. Lütken and G. G. Ross, Geometric scaling in the quantum Hall system, *Phys. Lett. B* **653**, 363 (2007).
- [18] C. A. Lütken and G. G. Ross, Implications of experimental probes of the RG-flow in quantum Hall systems, [arXiv:0906.5551v1](https://arxiv.org/abs/0906.5551v1) [cond-mat.other].
- [19] C. A. Lütken and G. G. Ross, On the origin of duality in the quantum Hall system, *Phys. Lett. A* **374**, 4700 (2010).
- [20] C. A. Lütken and G. G. Ross, Experimental probes of emergent symmetries in the quantum Hall system, *Nucl. Phys. B* **850**, 321 (2011).
- [21] B. P. Dolan, Holomorphic and anti-holomorphic conductivity flows in the quantum Hall effect, *J. Phys. A* **44**, 175001 (2011).
- [22] J. Nissinen and C. A. Lütken, Renormalization-group potential for quantum Hall effects, *Phys. Rev. B* **85**, 155123 (2012).
- [23] J. Nissinen and C. A. Lütken, The quantum Hall curve, [arXiv:1207.4693v1](https://arxiv.org/abs/1207.4693v1) [cond-mat.str-el].
- [24] C. A. Lütken and G. G. Ross, Quantum critical Hall exponents, *Phys. Lett. A* **378**, 262 (2014).
- [25] C. A. Lütken, Infinite symmetry in the quantum Hall effect, *EPJ Web of Conf.* **71**, 00079 (2014).
- [26] C. A. Lütken, Introduction to the role of modular symmetries in graphene and other two-dimensional materials, *Contemp. Phys.* **56**, 292 (2014).
- [27] R. B. Laughlin, M. L. Cohen, J. M. Kosterlitz, H. Levine, S. B. Libby, and A. M. M. Pruisken, Scaling of conductivities in the fractional quantum Hall effect, *Phys. Rev. B* **32**, 1311 (1985).
- [28] This has implications for the critical exponents (flow rates near saddle points), which are in agreement with experimental observations [16 and 24].
- [29] Not least of which is that the QHE implies Fermat's Last Theorem. A counter-example would allow the construction of an elliptic curve whose properties imply that a 2-form on  $\Gamma_0(2) = \Gamma_T$  must be a cusp form [30]. This contradicts the physics of the spin-polarized QHE, which has this symmetry, because the  $\beta$  function is not a cusp form.
- [30] F. Diamond and J. Schurman, *A First Course in Modular Forms*, Graduate Texts in Mathematics Vol. 228 (Springer-Verlag, New York, 2005).
- [31] H. Petersson, Über die Kongruenzgruppen der Stufe 4, *J. reine angew. Math.* **212**, 63 (1963).
- [32] R. Rankin, *Modular Forms and Functions* (Cambridge University Press, Cambridge, UK, 1977).
- [33] Other names for these groups are  $\Gamma_0(2) = \Gamma_T$ ,  $\Gamma^0(2) = \Gamma_R$ , and  $\Gamma_\theta(2) = \Gamma_S$ . Our simplified notation is similar to Ref. [32].
- [34] The number of weight two forms on the principal congruence subgroup  $\Gamma(N)$  is 2 for  $\Gamma(2)$ , and  $(N+6)N^2/24 \times \prod_{p|N} (1-p^{-2})$ , for primes  $p$  that divide  $N > 2$  [30]. The subscript will usually be suppressed, except when it is important to recall the dimension of this vector space.
- [35] D. Zagier, *The 1-2-3 of Modular Forms*, Lectures at a Summer School in Nordfjordeid, Norway, Annals of Mathematics Studies No. 97 (Springer-Verlag, Berlin, Heidelberg, 2008).
- [36] Y. Zhang, Z. Jiang, J. P. Small, M. S. Purewal, Y.-W. Tan, M. Fazlollahi, J. D. Chudow, J. A. Jaszczak, H. L. Stormer, and P. Kim, Landau-Level Splitting in Graphene in High Magnetic Fields, *Phys. Rev. Lett.* **96**, 136806 (2006).
- [37] J. G. Checkelsky, L. Li, and N. P. Ong, Zero-Energy State in Graphene in a High Magnetic Field, *Phys. Rev. Lett.* **100**, 206801 (2008).
- [38] The idea of finding a  $C$  function that interpolates between maximal symmetries first appeared in [4], but only phase diagrams for  $a = -1, 1/2, 1$ , and 2 were discussed in detail.
- [39] E. Fradkin, *Field Theories of Condensed Matter Physics* (Cambridge University Press, Cambridge, UK, 2013).
- [40] H. P. Wei, D. C. Tsui, and A. M. M. Pruisken, Localization and scaling in the quantum Hall regime, *Phys. Rev. B* **33**, 1488 (1986).
- [41] M. Z. Hasan and C. L. Kane, Topological insulators, *Rev. Mod. Phys.* **82**, 3045 (2010).
- [42] S. S. Murzin, S. I. Dorozhkin, D. K. Maude, and A. G. M. Jansen, Scaling flow diagram in the fractional quantum Hall regime of GaAs/Al<sub>x</sub>Ga<sub>1-x</sub>As heterostructures, *Phys. Rev. B* **72**, 195317 (2005).
- [43] W. Li, C. L. Vicente, J. S. Xia, W. Pan, D. C. Tsui, L. N. Pfeiffer, and K. W. West, Scaling in Plateau-to-Plateau Transition: A Direct Connection of Quantum Hall Systems with the Anderson Localization Model, *Phys. Rev. Lett.* **102**, 216801 (2009).
- [44] J. Wang, B. Lian, and S.-C. Zhang, Quantum anomalous Hall effect in magnetic topological insulators, *Phys. Scr.* **T164**, 014003 (2015).
- [45] Y. Ando, Topological insulator materials, *J. Phys. Soc. Jpn.* **82**, 102001 (2013).
- [46] J. G. Checkelsky, R. Yoshimi, A. Tsukazaki, K. S. Takahashi, Y. Kozuka, J. Falson, M. Kawasaki, and Y. Tokura, Trajectory of the anomalous Hall effect towards the quantized state in a ferromagnetic topological insulator, *Nat. Phys.* **10**, 731 (2014).
- [47] M. König, S. Wiedmann, C. Brune, A. Roth, H. Buhmann, L. W. Molenkamp, X.-L. Qi, and S.-C. Zhang, Quantum spin Hall insulator state in HgTe quantum wells, *Science* **318**, 766 (2007).

- [48] B. A. Bernevig, T. L. Hughes, and S.-C. Zhang, Quantum spin Hall effect and topological phase transition in HgTe quantum wells, *Science* **314**, 1757 (2006).
- [49] E. B. Olahanetsky, S. Sassine, Z. D. Kvon, N. N. Mikhailov, S. A. Dvoretzky, J. C. Portal, and A. L. Aseev, Quantum Hall liquid-insulator and plateau-to-plateau transitions in a high mobility 2DEG in a HgTe quantum well, *J. Exper. Theor. Phys. Lett.* **84**, 565 (2006).
- [50] Y. G. Arapov, S. V. Gudina, V. N. Neverov, S. M. Podgornykh, M. R. Popov, G. I. Harus, N. G. Shelushinina, M. V. Yakunin, N. N. Mikhailov, and S. A. Dvoretzky, Temperature scaling in the quantum-Hall-effect regime in a HgTe quantum well with an inverted energy spectrum, *Semiconductors* **49**, 1545 (2015).
- [51] S. V. Gudina, Y. G. Arapov, V. N. Neverov, S. M. Podgornykh, M. R. Popov, N. G. Shelushinina, M. V. Yakunin, S. A. Dvoretzky, and N. N. Mikhailov, 2D-localization and delocalization effects in quantum Hall regime in HgTe wide quantum wells, *Phys. Status Solidi C* **13**, 473 (2016).
- [52] R. Yoshimi, A. Tsukazaki, Y. Kozuka, J. Falson, K. S. Takahashi, J. G. Checkelsky, N. Nagaosa, M. Kawasaki, and Y. Tokura, Quantum Hall effect on top and bottom surface states of topological insulator  $(\text{Bi}_{1-x}\text{Sb}_x)_2\text{Te}_3$  films, *Nat. Commun.* **6**, 6627 (2015).
- [53] L. Li, F. Yang, G. J. Ye, Z. Zhang, Z. Zhu, W. Lou, X. Zhou, L. Li, K. Watanabe, T. Taniguchi, K. Chang, Y. Wang, X. H. Chen, and Y. Zhang, Quantum Hall effect in black phosphorus two-dimensional electron system, *Nat. Nanotechnol.* **11**, 593 (2016).
- [54] S. S. Murzin, M. Weiss, A. G. M. Jansen, and K. Eberl, Universal flow diagram for the magnetoconductance in disordered GaAs layers, *Phys. Rev. B* **66**, 233314 (2002).
- [55] L. I. Huang, Y. Yang, R. E. Elmquist, S. T. Lo, F. H. Liu, and C. T. Liang, Insulator-quantum Hall transition in monolayer epitaxial graphene, *RSC Adv.* **6**, 71977 (2016).
- [56] V. P. Gusynin and S. G. Sharapov, Unconventional Integer Quantum Hall Effect in Graphene, *Phys. Rev. Lett.* **95**, 146801 (2005).
- [57] Y. Zhang, H. L. Stormer, and P. Kim, Experimental observation of the quantum Hall effect and Berry's phase in graphene, *Nature (London)* **438**, 201 (2005).
- [58] X. Wu, M. Ruan, Y. Hu, N. K. Madiomanana, J. Hankinson, M. Sprinkle, C. Berger, and W. A. de Heer, Half integer quantum Hall effect in high mobility single layer epitaxial graphene, *Appl. Phys. Lett.* **95**, 223108 (2009).
- [59] M. Amado, E. Diez, F. Rossella, V. Bellani, D. Lopez-Romero, and D. M. Maude, Magneto-transport of graphene and quantum phase transitions in the quantum Hall regime, *J. Phys.: Condens. Matter* **24**, 305302 (2012).
- [60] K. S. Novoselov, A. Geim, S. Morozov, D. Jiang, M. I. Katsnelson, V. Grigorieva, and S. V. Dubonos, Two-dimensional gas of massless Dirac fermions in graphene, *Nature (London)* **438**, 197 (2005).
- [61] Y.-T. Wang, G.-H. Kim, C. F. Huang, S.-T. Lo, W.-J. Chen, J. T. Nicholls, L.-H. Lin, D. A. Ritchie, Y. H. Chang, C.-T. Liang, and B. P. Dolan, Probing temperature-driven flow lines in a gated two-dimensional electron gas with tunable spin-splitting, *J. Phys.: Condens. Matter* **24**, 405801 (2012).
- [62] X. Du, I. Skachko, F. Duerr, A. Lucian, and E. Y. Andrei, Fractional quantum Hall effect and insulating phase of Dirac electrons in graphene, *Nature (London)* **462**, 192 (2009).
- [63] K. I. Bolotin, F. Ghahari, M. D. Schulman, H. L. Stormer, and P. Kim, Observation of the fractional quantum Hall effect in graphene, *Nature (London)* **462**, 196 (2009).
- [64] B. E. Feldman, B. Krauss, J. H. Smet, and A. Yacoby, Unconventional sequence of fractional quantum Hall states in suspended graphene, *Science* **337**, 1196 (2012).
- [65] L. Zhang, Y. Zhang, M. Khodas, T. Valla, and I. A. Zaloznyak, Metal to Insulator Transition on the  $N = 0$  Landau Level in Graphene, *Phys. Rev. Lett.* **105**, 046804 (2010).
- [66] Z. Jiang, Y. Zhang, H. L. Stormer, and P. Kim, Quantum Hall States near the Charge-Neutral Dirac Point in Graphene, *Phys. Rev. Lett.* **99**, 106802 (2007).
- [67] The  $\Gamma(2)$ -invariant holomorphic function  $\lambda = \theta_2^4/\theta_3^4$  is also known as the *hauptmodul* for the *modular curve*  $X(2) = \mathbb{C}^+/\Gamma(2)$ .
- [68] It is highly unusual to have a universal form of the RG potential beyond leading order in an expansion near a critical point. The scheme independence encountered here is a consequence of the draconian constraints enforced by the holomorphic modular structure.
- [69] D. E. Khmel'nitzkii, Quantization of Hall conductivity, *J. Exper. Theor. Phys. Lett.* **38**, 552 (1983).
- [70] H. Levine, S. B. Libby, and A. M. M. Pruisken, Electron Delocalization by a Magnetic Field in Two Dimensions, *Phys. Rev. Lett.* **51**, 1915 (1983).
- [71] A. M. M. Pruisken, On localization in the theory of the quantized Hall effect: A two-dimensional realization of the  $\theta$ -vacuum, *Nucl. Phys. B* **235**, 277 (1984).
- [72] H. Levine, S. B. Libby, and A. M. M. Pruisken, Theory of the quantized Hall effect (I), *Nucl. Phys. B* **240**, 30 (1984).
- [73] H. Levine, S. B. Libby, and A. M. M. Pruisken, Theory of the quantized Hall effect (II), *Nucl. Phys. B* **240**, 49 (1984).
- [74] H. Levine, S. B. Libby, and A. M. M. Pruisken, Theory of the quantized Hall effect (III), *Nucl. Phys. B* **240**, 71 (1984).
- [75] A. M. M. Pruisken, Dilute instanton gas as the precursor to the integral quantum Hall effect, *Phys. Rev. B* **32**, 2636 (1985).
- [76] A. M. M. Pruisken, Universal Singularities in the Integral Quantum Hall Effect, *Phys. Rev. Lett.* **61**, 1297 (1988).
- [77] S.-C. Zhang, T. H. Hansson, and S. Kivelson, Effective-Field-Theory Model for the Fractional Quantum Hall Effect, *Phys. Rev. Lett.* **62**, 82 (1989).
- [78] D.-H. Lee, S. Kivelson, and S.-C. Zhang, Quasi-Particle Charge and Activated Conductance of a Quantum Hall Liquid, *Phys. Rev. Lett.* **68**, 2386 (1992).
- [79] S. Kivelson, D.-H. Lee, and S.-C. Zhang, Global phase diagram in the quantum Hall effect, *Phys. Rev. B* **46**, 2223 (1992).
- [80] E. Shimshoni, S. L. Sondhi, and D. Shahar, Duality near quantum Hall transitions, *Phys. Rev. B* **55**, 13730 (1997).
- [81] X. G. Wen and A. Zee, Classification of Abelian quantum Hall states and matrix formulation of topological fluids, *Phys. Rev. B* **46**, 2290 (1992).
- [82] J. K. Jain, Theory of the fractional quantum Hall effect, *Phys. Rev. B* **41**, 7653 (1990).